AGU ADVANCING EARTH AND SPACE SCIENCES

Water Resources Research

RESEARCH ARTICLE
10.1029/2025WR042447

Near-Bed Flow Turbulence Beneath Ice Cover Under Varying Hydrological Conditions: A 9-Year Field Measurement-Based Analysis From a Meander Bend

Karoliina Lintunen[1], Essi Vilhonen[1], Tuure Takala[2], Linnea Blåfield[1], Elina Kasvi[1], Eliisa Lotsari[2,3], and Petteri Alho[1]

[1]Department of Geography and Geology, University of Turku, Turku, Finland, [2]Department of Built Environment, Water and Environmental Engineering, Aalto University, Aalto, Finland, [3]Department of Geographical and Historical Studies, University of Eastern Finland, Joensuu, Finland

Key Points:

- Water column height beneath ice is the main control of near-bed turbulence, with turbulence decreasing as height increases
- Ice cover formation conditions influence the water column height and therefore affect near-bed turbulence
- Discharge affects near-bed turbulence, with low and moderate flows strengthening the influence of ice whereas high flows reduce it

Correspondence to:
K. Lintunen,
emklin@utu.fi

Citation:
Lintunen, K., Vilhonen, E., Takala, T., Blåfield, L., Kasvi, E., Lotsari, E., & Alho, P. (2026). Near-bed flow turbulence beneath ice cover under varying hydrological conditions: A 9-year field measurement-based analysis from a meander bend. *Water Resources Research*, *62*, e2025WR042447. https://doi.org/10.1029/2025WR042447

Received 29 SEP 2025
Accepted 23 FEB 2026

Author Contributions:
Conceptualization: Karoliina Lintunen, Eliisa Lotsari
Data curation: Karoliina Lintunen, Essi Vilhonen, Tuure Takala, Eliisa Lotsari
Formal analysis: Karoliina Lintunen, Essi Vilhonen, Tuure Takala
Funding acquisition: Karoliina Lintunen, Elina Kasvi, Eliisa Lotsari, Petteri Alho
Investigation: Karoliina Lintunen, Tuure Takala, Linnea Blåfield, Elina Kasvi, Eliisa Lotsari, Petteri Alho
Methodology: Karoliina Lintunen, Essi Vilhonen
Project administration: Karoliina Lintunen
Software: Karoliina Lintunen, Essi Vilhonen
Supervision: Elina Kasvi, Eliisa Lotsari, Petteri Alho
Validation: Karoliina Lintunen, Essi Vilhonen

Abstract Climate change alters hydrological and ice conditions, but how these changes affect turbulence beneath ice cover has been poorly studied. This study presents a multi-year observational analysis of near-bed turbulence under ice cover in a subarctic meandering river reach. Measurements were obtained using an Acoustic Doppler Current Profiler (ADCP) and an Acoustic Doppler Velocimeter (ADV), which provided flow parameters and enabled the calculation of turbulence variables, together with a camera to capture visual information on bedforms. In the analyses, we considered the effects of water column height, ice thickness, discharge, and riverbed forms on near-bed turbulence. The results show that water column height beneath ice cover is the most consistent factor controlling turbulence because near-bed turbulence generally decreases as the water column height increases. Conditions during ice formation affected the resulting water column height and thus indirectly influenced near-bed turbulence. Turbulence was most pronounced in shallow upstream and inner-bend sections of the meander whereas deeper areas exhibited reduced turbulence. Discharge modulated the ice effect, with low to moderate winter flows amplifying ice's influence on near-bed turbulence whereas higher flows tended to override it. Thicker ice cover was associated with reduced turbulent kinetic energy (TKE) but with increased streamwise and vertical turbulence intensities during low-flow years. These results suggest that ongoing shifts in winter ice regimes and flow seasonality may alter under-ice turbulence, with consequent effects on sediment transport and channel morphodynamics. Uncertainty in comparisons arises from instrument limitations, field conditions, and interannual variability in hydrological regimes.

1. Introduction

Approximately half of Earth's rivers experience ice cover at some point during the hydrological year (Bennett & Prowse, 2010) and these rivers drain over one-third of the Earth's landmass (Yang et al., 2020). River ice is an important factor affecting alluvial rivers across various spatial and temporal scales (Ettema, 2002; Shen, 2025), especially in the high-latitude regions, where ice cover can be present for up to 8–9 months annually. Due to global climate change, the duration of winter seasons is shortening, particularly in high-latitude regions, where surface air temperatures are increasing (Huang et al., 2017; Shen, 2025; Wang et al., 2021). Consequently, rivers' ice-covered seasons have been observed to shorten (Fukś, 2023; Newton & Mullan, 2021; Yang et al., 2020), accompanied by shifts in river flow seasonality (Wang et al., 2024). The changes in the winter conditions are predicted to accelerate (Newton & Mullan, 2021) and the decline in river ice extent is expected to continue with global warming (Yang et al., 2020). Changes in mid-winter and ice conditions affect the hydraulics and turbulence of the flow, which in turn play a critical role in the sediment transport (Dey, 2014).

In fluid flow, turbulence is defined by the irregular and chaotic movement of fluid particles, with their velocities varying in space and time (Dey, 2014). Turbulence involves chaotic three-dimensional velocity fluctuations layered on top of the average flow. The characteristics of turbulent flow depend on the boundary conditions, and in open-channel flow, the interaction between the flow and the channel bed primarily controls turbulence (Dey, 2014; Kumar et al., 2025). However, in ice-covered rivers, ice cover introduces an additional roughness boundary, altering flow dynamics and modifying turbulence compared to open channels (Ettema & Daly, 2004; Robert & Tran, 2012; Sukhodolov et al., 1999). An ice-covered channel can be divided into two distinct parts: one where the flow is influenced by the riverbed and the other where it is influenced by the ice cover (Larsen, 1966). Flow turbulence characteristics can be quantified using various metrics (i.e., turbulent kinetic energy (TKE),

Visualization: Essi Vilhonen
Writing – original draft: Karoliina Lintunen, Essi Vilhonen
Writing – review & editing: Karoliina Lintunen, Essi Vilhonen, Linnea Blåfield, Elina Kasvi, Eliisa Lotsari, Petteri Alho

turbulence intensity (TI), and Reynolds shear stress (τ_{ij} for $i \neq j$)). TKE represents the amount of energy within the turbulent fluctuations of the flow, and TI is the ratio of these turbulent fluctuations to the average flow velocity. Reynolds shear stress measures the stress caused by the turbulent shear forces in the flow. The roughness of the riverbed and the ice cover influence turbulence; smoother surfaces tend to reduce turbulence whereas rougher surfaces increase it. These factors lead to modifications in velocity profiles (Koyuncu & Le, 2022), shear stress (Robert & Tran, 2012), and sediment transport (Turcotte et al., 2011).

Turbulence in ice-covered rivers has been studied with analytical models (Wang et al., 2021), hydrodynamic modeling (Lotsari, Tarsa, et al., 2019; Smith et al., 2023), flume studies (Barahimi & Sui, 2024; Behera et al., 2023; Kumar et al., 2025; Muste et al., 2000; Robert & Tran, 2012), and field observations using acoustic instruments such as acoustic Doppler current profilers (ADCPs) and acoustic Doppler velocimeters (ADVs) (Demers et al., 2011; Koyuncu & Le, 2022; Lotsari et al., 2020; Sukhodolov et al., 1999; Wilcox & Wohl, 2006). These studies show how ice cover, bedforms, vegetation, and seepage alter turbulence, shear stress, and sediment dynamics. For example, ice cover increases flow depth and redistributes turbulence (Muste et al., 2000), rough ice undersides elevate turbulence and shear stress (Robert & Tran, 2012), and vegetation or seepage can restructure near-bed turbulence (Barahimi & Sui, 2024; Behera et al., 2023). Field measurements emphasize ice's influence on turbulence structures (Demers et al., 2013; Lotsari et al., 2020), yet progress remains limited by the difficulty of winter data collection and the need for better integration of ADCP and ADV observations (Koyuncu & Le, 2022).

Open-channel flow conditions depend on the channel geometry, geomorphology, and hydraulic properties of moving water. These factors also explain flow processes beneath ice, but ice cover further modifies the dynamics (Ghareh Aghaji Zare et al., 2016; Muste et al., 2000; Prowse, 2001). Under ice cover, flow is influenced by the differing roughnesses of the ice underside and the riverbed. Ice cover alters hydraulics by adding an upper boundary layer, modifying velocity distribution, and raising water levels compared to open flow (Beltaos, 2008; Sui et al., 2010; Teal et al., 1994).

Flow beneath ice is turbulent, asymmetric, and fully developed, with boundary-generated turbulence mixing through the water column, especially in the central core (Chen et al., 2018; Guo et al., 2017; Muste et al., 2000). The maximum velocity occurs approximately midway between the channel bed and the ice cover, whereas in an open channel, the maximum velocities occur near the surface (Demers et al., 2013; Lotsari et al., 2017). The ice cover slows the near-surface flow due to friction (Sukhodolov et al., 1999), enhances the channel's resistance to flow, and decreases sediment transport capacity (Ettema, 2008). It also affects lateral variations in the depth of maximum flow and boundary shear stresses, promoting flow concentration along the thalweg (Ettema & Kempema, 2012; Lotsari, Tarsa, et al., 2019; Lotsari et al., 2017).

Previous research shows that near-bed turbulence beneath ice cover is controlled by interactions between the channel bed and the ice underside. Important factors include relative roughness, altered velocity gradients, and coherent structures, such as sweeps and ejections, which affect turbulence intensity, Reynolds stresses, and sediment entrainment, even during low-flow winters (Ettema & Daly, 2004; Lotsari et al., 2020; Robert & Tran, 2012; Sukhodolov et al., 1999). Although rough ice can generate localized turbulence, overall turbulence remains lower than in open water due to generally lower discharge conditions. Hence, under ice cover, both increased viscosity and ice cover underside roughness alter turbulence intensity and the distribution of Reynolds stresses.

Low water temperature and river ice cover during mid-winter conditions increase the wetted perimeter of the channel and affect sediment transport, channel geometry, and flow properties (Ettema, 2002; Muste et al., 2000; Sui et al., 2010; Teal et al., 1994). When water temperature decreases to 0°C, kinematic viscosity increases (Turcotte et al., 2011), which increases flow drag on the bed while reducing the fall velocity of suspended particles (Ettema, 2008). As viscosity changes with temperature, the thickness of the laminar sublayer also adjusts, altering the relative roughness of the bed and the forces acting on bed sediment particles; consequently, sediment transport generally increases as water temperature decreases (Shen, 2025).

Low water temperature additionally promotes frazil and anchor-ice formation, which can bind bed material and raft it downstream, further enhancing sediment movement during the freeze-up phase (Turcotte et al., 2011). Although sediment transport is traditionally assumed to decrease during winter due to reduced runoff and flow (Ettema, 2002), recent studies suggest that sediment transport beneath ice cover may be more significant than previously thought (Koyuncu & Le, 2020, 2022; Lotsari et al., 2017; Turcotte et al., 2011).

Although studies have highlighted ice cover's influence on turbulence, important knowledge gaps remain. Currently, there are no studies in which near-bed flow turbulence has been detected over almost a decade of mid-winter conditions in a subarctic river. Knowledge gaps remain concerning the temporal and longitudinal variability of turbulence over the ice-covered season, the role of evolving ice-cover roughness in shaping near-bed flow, and the coupling between high-frequency turbulence metrics and sediment transport in natural rivers (Ettema & Daly, 2004; Lotsari, Tarsa, et al., 2019; Turcotte et al., 2011). Addressing these gaps through long-term, field-based research is necessary to advance understanding of ice-flow interactions under changing winter conditions.

This study is based on under-ice measurements conducted annually from 2016 to 2024 in a meander bend of the Pulmanki River, located in northern Finnish Lapland. The aim of this paper is to (a) analyze near-bed flow turbulence parameters (i.e., Reynolds shear stress, turbulence intensity and turbulent kinetic energy) within a meander bend during various hydrological mid-winter conditions and (b) study how various bedform structures affect these near-bed flow turbulence parameters below ice cover. The analyses are based on ADCP and ADV measurements conducted once annually under varying mid-winter conditions over a 9-year period, supplemented by a once-conducted visual survey of the bedforms. The turbulence of the near-bed flow was measured in the closest possible proximity to the riverbed. Statistical and visual methods were used to analyze the data. Measurements collected over multiple years provide a comprehensive understanding of how variations in flow, ice conditions, and bedforms influence turbulence characteristics. This study's results increase the knowledge of river ice processes and help researchers better quantify the impacts of climate change and the effects of river ice cover loss.

2. Study Area

The Pulmanki River, a 58-km tributary of the Tana River, is located in northern Finnish Lapland and divided into upper and lower sections by Lake Pulmanki (Alho & Mäkinen, 2010). The region is classified as “cold, without dry season, but with cold summer” (Peel et al., 2007) in the Köppen climate classification, with weather influenced by the Atlantic Ocean, the Gulf Stream, and the Asian continent (Autio & Heikkinen, 2002). The Pulmanki River flows through a glaciofluvial deposit valley where the materials were deposited during the retreat of the continental ice (Mansikkaniemi & Mäki, 1990). The study area is a simple symmetric meander bend in the meandering upper Pulmanki River (Figure 1). The bend's apex has a radius of curvature of 110 m (Lotsari et al., 2014). During wintertime, the width of the bend is approximately 25 m at the widest (CS1 and CSA), with typical mean width between 10 and 15 m (CS2–CS4).

The Pulmanki River experiences annual peak discharges typically from mid-May to early June, coinciding with the spring snowmelt flood, with flow rates increasing up to 80 m^3/s (Blåfield et al., 2024; Kasvi et al., 2015). In summer, discharge rates drop to about 4 m^3/s, declining further in autumn (Lotsari, Lind, et al., 2019). An ice-covered period typically starts in October, as temperatures drop below 0°C, lasting until April or May, when increasing solar radiation raises daytime temperatures above 0°C. During this ice-covered period, discharges are usually below 2 m^3/s and the ice cover is characterized as smooth-rough based on visual analyses conducted during the 2014 and subsequent field campaigns (Kämäri et al., 2017; Lotsari, Lind, et al., 2019). The reach has a predominantly sandy bed, with year-round sediment transport occurring both in suspension and as bedload, the latter being the dominant transportation form, and peak rates occurring during the spring floods (Kasvi et al., 2015, 2019; Lotsari et al., 2020). The riverbed is highly dynamic, and a single flood event can substantially alter its geometry. Sediment samples collected in 2020 and 2021 showed median particle sizes (D_{50}) ranging from 0.42 to 0.78 mm, with the highest bedload values recorded in 2020 at the bend outlet and lower values at the bend inlet and apex (Lotsari et al., 2020, 2022). Studies from the study site have shown that the studied bend mainly erodes under open-channel conditions and tends to experience deposition during the winter (Lotsari, Tarsa, et al., 2019). Therefore, near-bed flow velocities of magnitudes up to approximately 0.35 m/s move bedload during the coldest mid-winter conditions at the site (Lotsari et al., 2022) and continuous sediment transport has been documented throughout the year (Välimäki et al., 2025).

3. Data and Methods

3.1. Field Measurements of Cross-Sectional Profiles, Hydrology, and Bedform Conditions

Measurements were collected at seven cross-sectional profiles along the studied meander bend (Figure 1). Cross-section locations were mapped with RTK-GNSS, using 2016 reference points to ensure consistency across years.

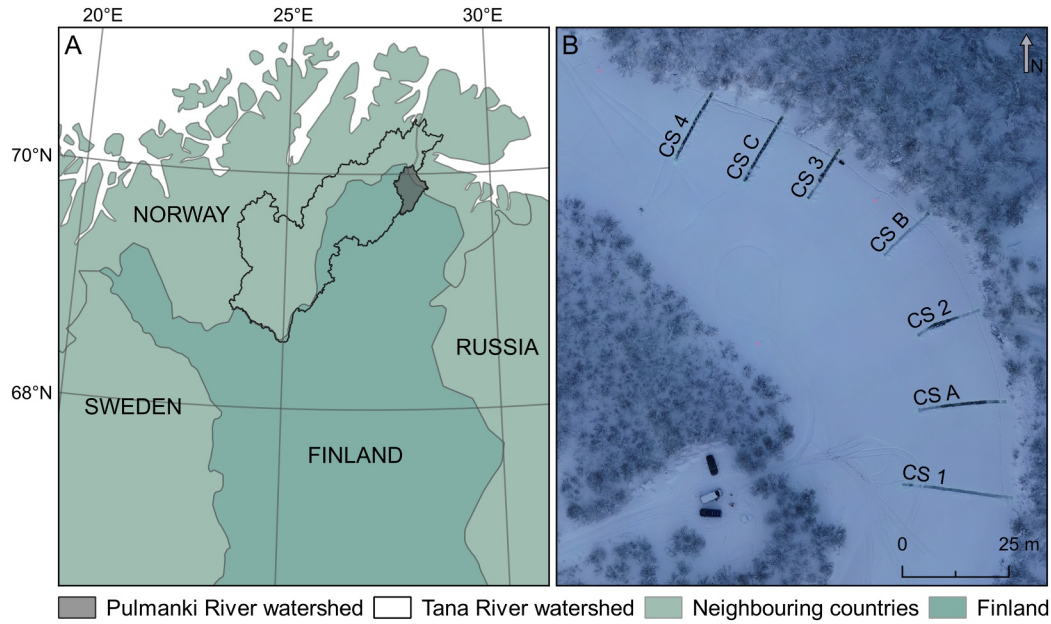

Figure 1. Location of the Pulmanki River watershed (a) and view of the studied meander bend and its seven measurement cross-sections (b). Flow direction is from CS1 toward CS4.

Each cross-section was oriented perpendicular to the flow, and measurement holes were drilled through the ice at ~1-m intervals with an ice auger (Figure 2). At each hole, ice thickness and total water depth (riverbed to ice surface) were recorded (Table 1). Water column height beneath the ice cover was later calculated by extracting measured ice cover thickness from total water depth (i.e., the distance from ice cover surface to riverbed). Annual discharges were determined based on stationary ADCP cross-section measurements (Table 2; see chapter 3.2). Annual variation in cross-section depth profiles reflects erosional processes occurring throughout the year (Figure 3).

Freeze-thaw indicators were calculated based on the thermal winter starting date (date when mean temperature of the day falls permanently below 0°C) and temperature data from the Nuorgam weather station, provided by the Finnish Meteorological Institute (FMI). The date of stable ice cover formation was determined from daily game camera photos taken 2 km upstream of the study site (Lotsari, Lind, et al., 2019). At the camera location, the channel is steeper and shallower and has a higher flow velocity than at our study site and therefore tends to freeze later. Consequently, the stable ice cover date is used only as an indicative parameter to describe hydrological conditions.

In 2024, additional data on small-scale bedforms were collected and compared to calculated turbulence conditions. The bedform data were gathered from all drill holes visually using a GoPro camera and a measuring rod. The camera was attached to the measuring rod with a ruler to obtain a reference for sediment sizes. The conditions beneath the ice were documented at each drill hole by filming the riverbed and its surrounding areas. When the surroundings were video-recorded, the measuring rod was rotated 360° to capture the overview. These videos provided insights into riverbed grain sizes and small-scale bedform structures. The collected data were visually analyzed and classified to describe 2024 riverbed topography. The cross-sectional classification is presented in the results section and compared with turbulence values.

3.2. Near-Bed Flow Measurement Methodology

From 2016 to 2024 near-bed flow was measured using an ADCP (Sontek M9). Between 2020 and 2024, an ADV (FlowTracker and FlowTracker2 with 2D or 3D probes) was also used (Table 2). ADCP and ADV measurements were conducted from the same drill holes, where the thickness of the ice cover and the water column height were measured (Figure 3).

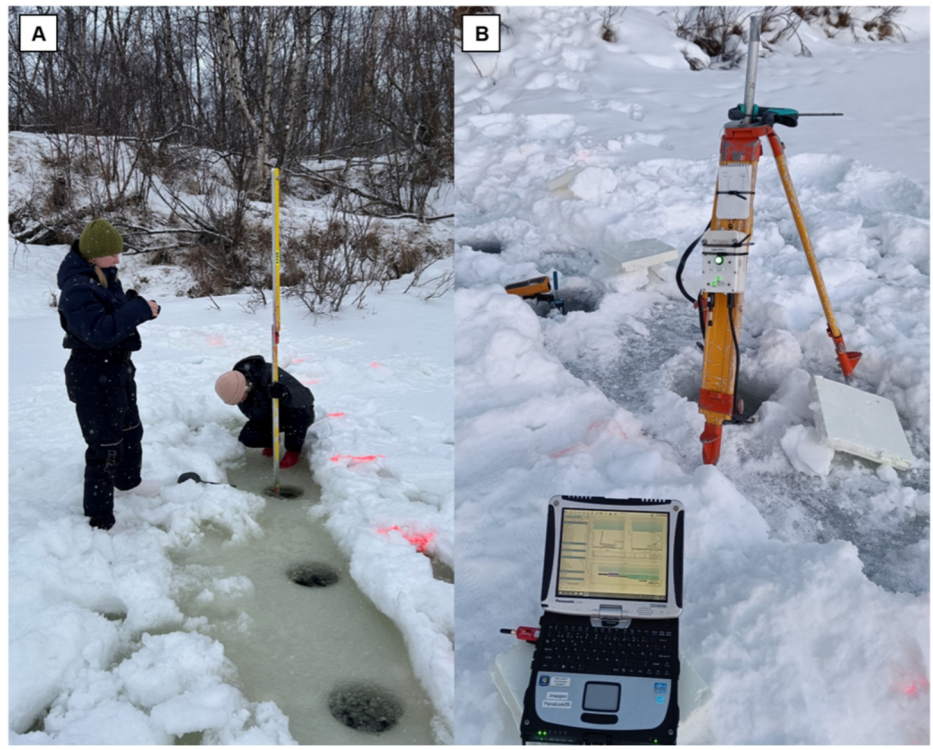

Figure 2. Example of field measurements. In part A, researchers are measuring ice cover thickness and depth of the drill hole, and part B shows the ADCP measurement setup of stationary measurements (B). The drill hole's depth is measured from the ice surface to the riverbed and the ice cover thickness from the underside of the ice to the surface. The height of the water column beneath the ice cover is later calculated by subtracting the measured ice cover thickness from the drill hole depth.

The M9 sensor features four beams at 3.0 MHz and four at 1.5 MHz, achieving an accuracy of ±0.25% of the measured velocity, or ±0.2 cm/s (SonTek, 2022). In this study, the ADCP sensor was used in stationary mode to gather velocity data at each drill hole. The ADCP sensor was mounted on a metal rod, and the measurements were taken at the water interface beneath the ice cover. The tagline azimuth was set at the first drill hole (i.e., at the left bank, closest to the point bar) in each cross-section, and the ADCP transducer depth was set to 0 m to optimize vertical flow measurement, accounting for ice cover and riverbed effects.

Table 1
Hydrological Variables of the Study Site During Field Campaigns

Measurement date	Discharge (m^3/s)	Water column height (m) (mean ± variation)	Ice cover thickness (m) (mean ± variation)
16.02.2016	1.38	0.42 (0.18–0.8)	0.44 (0.32–0.53)
16.02.2017	1.32	0.49 (0.21–1.25)	0.43 (0.25–0.54)
09.02.2018	0.18	0.34 (0.05–0.87)	0.39 (0.15–0.55)
07.02.2019	0.61	0.49 (0.2–1.47)	0.35 (0.25–0.48)
05.02.2020	0.79	0.42 (0.22–0.8)	0.38 (0.28–0.45)
15.02.2021	0.5	0.44 (0.2–1.15)	0.43 (0.32–0.65)
21.02.2022	0.67	0.49 (0.23–1.1)	0.58 (0.43–0.68)
21.02.2023	0.99	0.51 (0.25–1.22)	0.4 (0.32–0.46)
16.02.2024	0.76	0.59 (0.23–1.17)	0.52 (0.38–0.63)

Note. The mean water column heights and ice cover thicknesses were calculated from all cross-sections, and discharge was defined based on stationary ADCP cross-section measurements.

Table 2
Flow Measurement Dates, Equipment Used, and Surveyed Cross-Sections

Measurement date	ADCP (Sontek M9)	ADV (FlowTracker 2D)	ADV (FlowTracker 3D)
16.02.2016	CS1-CS4		
16.02.2017	CS1-CS4		
09.02.2018	CS1-CS4		
07.02.2019	CS1-CS4		
05.02.2020	CS1-CS4		CS1, CS2, CS3, CS4, every other drill hole
15.02.2021	CS1-CS4	CS1, CS2, CS3, CS4	
21.02.2022	CS1-CS4	CS1-CS4	
21.02.2023	CS1-CS4		CS1-CS4
16.02.2024	CS1-CS4		CS1-CS4

Due to bed interference, the ADCP cannot measure the lowest part of the water column (Lentz et al., 2022). In addition, stationary flow measurements cannot be conducted if the water column height below the ADCP sensors transducer is less than 25 cm due to the minimum profiling range (20 cm) and blanking distance (5 cm) (SonTek, 2022). To address these issues, ADV measurements were taken during field campaigns from 2020 to 2024 from near the riverbed, using the same drill holes and cross-sections where possible. ADV measurements were made by positioning the probe approximately 4 cm above the bed. The probe is 5 cm in vertical height, with a sampling volume extending 10 cm from the probe tip (SonTek, 2019). Each measurement lasted 50 s (2020), 60 s (2021), or 120 s (2022–2024) and was conducted with a 2D or 3D probe, depending on the ADV instrument available (Table 2). Measurement duration was standardised to 120 s from 2022 following an instrument change that enabled longer measurements under freezing conditions. Lotsari et al. (2022) provide more detailed data and measurement procedures.

3.3. The Analyses of the Near-Bed Turbulence Parameters in an Ice-Covered Channel

Near-bed flow turbulence conditions at each cross-section were compared annually and individually, considering variations in hydrological conditions. The ADV flow velocities were measured in a coordinate system with the x-axis perpendicular to the tagline, the y-axis along the tagline and, in the case of 3D measurements, the z-axis pointing vertically upwards, resulting in velocity components v_1, v_2, and v_3, respectively. The ADCP flow velocities were measured in *ENU* (east, north, up) coordinates, and the corresponding velocity components are again denoted as v_1, v_2, and v_3, respectively. To obtain the streamwise (u) and cross-stream (v) velocity components, the velocities v_1 and v_2, measured in the streamwise plane, are rotated counterclockwise by an angle, α, denoting the counterclockwise angle between v_1 and the total planar velocity:

$$u = v_1 \cos(\alpha) - v_2 \sin(\alpha) \tag{1}$$

$$v = v_1 \sin(\alpha) + v_2 \cos(\alpha) \tag{2}$$

for each timestep. Additionally, $w = v_3$ (i.e., the third measured velocity is already in the upward direction in both sets of measurements). The average speed is calculated as $\sqrt{\overline{u}^2 + \overline{v}^2 + \overline{w}^2}$ (Wilcox & Wohl, 2006).

3.3.1. Analysis of Turbulence Parameters From ADV Data

To estimate turbulence production under the ice cover, we calculate turbulent kinetic energy as (Groom & Friedrich, 2019; Jamieson et al., 2010)

$$\mathrm{TKE} = \frac{1}{2}\left(\overline{(u')^2} + \overline{(v')^2} + \overline{(w')^2}\right) \tag{3}$$

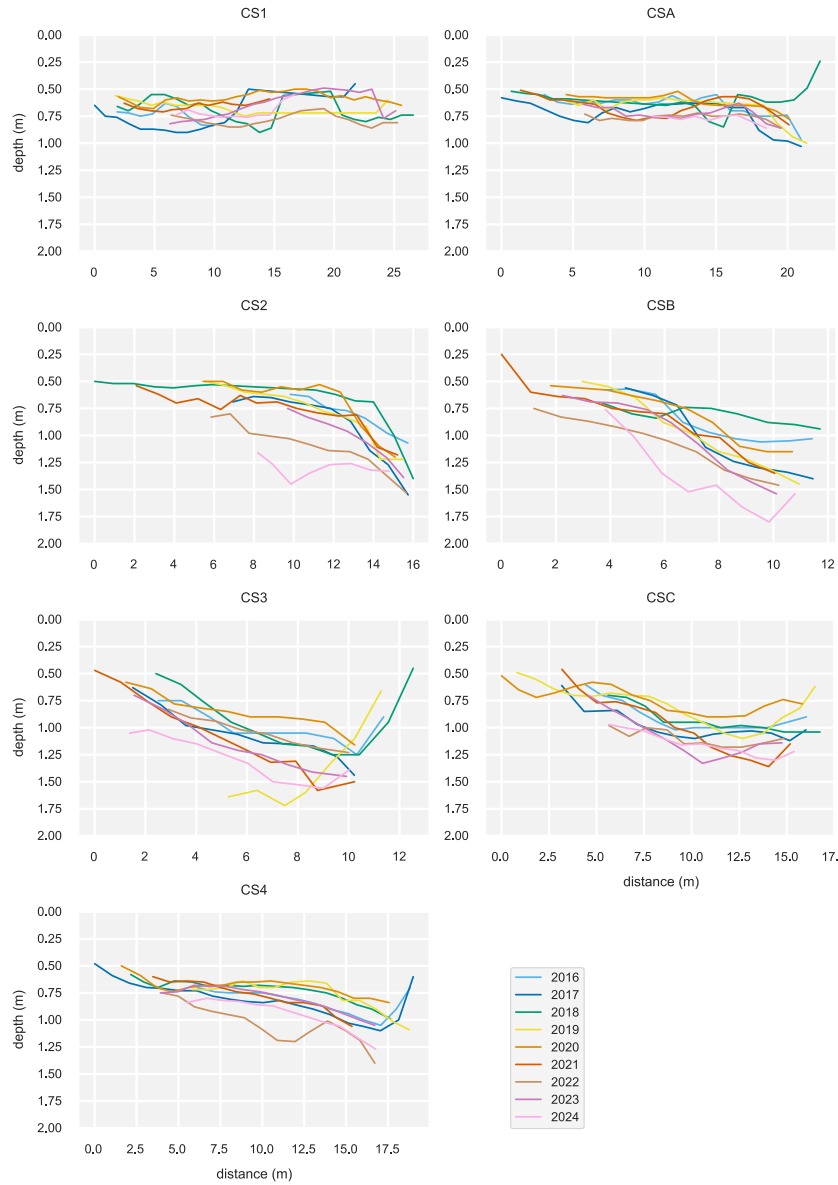

Figure 3. Depth profiles of cross-sections during the studied years. Upstream cross-sections (CS1-CSA) were typically the shallowest and widest whereas in the apex section (CS2-CS3), depth profiles deepened toward the outer bank and cross-sections were narrower. In the outlet cross-sections (CSC-CS4), depths were shallower and the depth profiles had gentler slopes toward the outer bank than in the apex.

where overbars denote time averages and u', v' and w' are the fluctuating components of the streamwise (u), cross-stream (v), and vertical (w) components of the flow velocity, respectively. They are obtained from the full-velocity components, u, v, and w, at each timestep by subtracting the mean:

$$u'(x,t) = u(x,t) - \overline{u(x)} \tag{4}$$

$$v'(x,t) = v(x,t) - \overline{v(x)} \tag{5}$$

$$w'(x,t) = w(x,t) - \overline{w(x)} \tag{6}$$

Further, we evaluate the Reynolds shear stress (τ) components (Jamieson et al., 2010):

$$\tau_{uv} = -\rho\overline{u'v'} \tag{7}$$

$$\tau_{uw} = -\rho\overline{u'w'} \tag{8}$$

$$\tau_{vw} = -\rho\overline{v'w'} \tag{9}$$

where ρ is the density of water (1000 kg/m^3), and again, overbars denote time averages.

To supplement the kinetic energy and shear stress results, we also present values for turbulence intensities (TI), which are calculated as root mean square of the fluctuating components (Groom & Friedrich, 2019):

$$\mathrm{TI}_u = \frac{\sqrt{\overline{(u')^2}}}{\overline{u}} \tag{10}$$

$$\mathrm{TI}_v = \frac{\sqrt{\overline{(v')^2}}}{\overline{v}} \tag{11}$$

$$\mathrm{TI}_w = \frac{\sqrt{\overline{(w')^2}}}{\overline{w}} \tag{12}$$

where turbulence intensities in each direction are normalized with the corresponding mean velocity components at each measurement site.

3.3.2. Analysis of Turbulence Parameters From ADCP Data

Because the ADCP measurement device measures the fluid velocities using four beams, we can reliably measure only quantities that can be expressed in terms of the beam velocities, b_i (De Serio & Mossa, 2015; Gilcoto et al., 2009; Stacey et al., 1999). Following De Serio and Mossa (2015), the velocity components (u, v, w) can be expressed as

$$u = \frac{b_1 - b_2}{2\sin\vartheta} \tag{13}$$

$$v = \frac{b_3 - b_4}{2\sin\vartheta} \tag{14}$$

$$w = \frac{b_1 + b_2 + b_3 + b_4}{4\cos\vartheta} \tag{15}$$

where ϑ is the opening angle of the device configuration, in our case 25° (SonTek, 2013). The above equations allow us to calculate the average velocities of the flow. Additionally, shear stresses can be computed using beam velocity (b'$_{1\text{-}4}$) variances (De Serio & Mossa, 2015) as

$$\overline{(b_1')^2} = \overline{u'^2}\sin^2\vartheta + \overline{u'w'}\sin\vartheta\cos\vartheta + \overline{w'^2}\cos^2\vartheta \tag{16}$$

$$\overline{(b_2')^2} = \overline{u'^2}\sin^2\vartheta - \overline{u'w'}\sin\vartheta\cos\vartheta + \overline{w'^2}\cos^2\vartheta \tag{17}$$

$$\overline{(b_3')^2} = \overline{v'^2}\sin^2\vartheta + \overline{v'w'}\sin\vartheta\cos\vartheta + \overline{w'^2}\cos^2\vartheta \tag{18}$$

$$\overline{(b_4')^2} = \overline{v'^2}\sin^2\vartheta - \overline{v'w'}\sin\vartheta\cos\vartheta + \overline{w'^2}\cos^2\vartheta \tag{19}$$

from which we obtain (De Serio & Mossa, 2015)

$$\tau_{uw} = -\rho\overline{u'w'} = -\rho\frac{\overline{(b_1')^2} - \overline{(b_2')^2}}{4\sin\vartheta\cos\vartheta} \tag{20}$$

$$\tau_{vw} = -\rho\overline{v'w'} = -\rho\frac{\overline{(b_3')^2} - \overline{(b_4')^2}}{4\sin\vartheta\cos\vartheta} \tag{21}$$

We note that, looking at the beam velocity and beam velocity variance formulae, there is no way to express u', v', and w' as functions of only the beam velocities and the opening angle; therefore, we cannot calculate TKE, TI:s, or τ_{uw}. However, we can write a lower bound (i.e., minimum) estimate for turbulent kinetic energy as (De Serio & Mossa, 2015)

$$\begin{aligned}\mathrm{TKE}_{\min} &= \frac{3}{8}\left(\overline{(b_1')^2} + \overline{(b_2')^2} + \overline{(b_3')^2} + \overline{(b_4')^2}\right) \\ &= \frac{3}{4}\left(\left(\overline{(u')^2} + \overline{(v')^2}\right)\sin^2\vartheta + \overline{(w')^2}\cos^2\vartheta\right)\end{aligned} \tag{22}$$

3.4. Performance of the ADCP and ADV in Measuring Flow Turbulence

In the case of ADV measurements, data from 2020, 2021, and 2024 were collected using the FlowTracker 3D instrument (Table 3), allowing all turbulence parameters to be computed. In 2022 and 2023, FlowTracker 2D was used, which did not measure the vertical velocity component (w). Consequently, TKE and the parameters τ_{uw}, τ_{vw}, and TI_w could not be calculated for those 2 years. For all years, average velocity components and Reynolds shear stresses can be calculated from the ADCP data whereas only a lower-bound estimate of TKE ($\mathrm{TKE}_{\min}$) is possible and turbulence intensities and full TKE cannot be determined.

Several studies have been conducted to examine flow turbulence using an ADCP and an ADV in laboratory and natural environments. As Nystrom et al. (2007) outlined, ADCPs, such as those used in this study, effectively reproduce mean velocity profiles. They found that, compared to ADV measurements, four-beam ADCPs resulted in equally accurate Reynolds stress estimates, provided that measurements were taken sufficiently far above the flume bottom boundary. However, TKE values were overestimated by more than a factor of two when ADCPs were used relative to ADV. This overestimation was linked to the methodological approach that they used for calculating TKE, which required assumptions of flow homogeneity and anisotropy. In contrast, in this study, we follow the convention De Serio and Mossa (2015) used for defining a lower-bound estimate for TKE, which results in TKE values that are significantly reduced compared to the corresponding TKE values from ADV measurements. Although ADCPs were generally prone to error near the bed, Nystrom et al., 2007 noted that in field conditions, ADCPs might better capture turbulence parameters and recommended further field-based investigations. In their review, Das and Debnath (2025) concluded that although ADVs provide higher spatial resolution and are effective for measuring turbulence, their accuracy can be affected by noise contamination. When studying ice-covered rivers, ADV instruments provide high-resolution, point-based measurements, making them well suited for capturing detailed turbulence characteristics at specific locations, for example, near the riverbed. However, collecting measurements throughout the entire water column with an ADV is time-consuming and inefficient. In contrast, ADCPs measure flow conditions throughout the entire water column, enabling large-scale field surveys to be conducted more quickly and efficiently, particularly in cold environments where fieldwork is challenging due to prevailing weather conditions. Although ADCPs can capture full velocity profiles, they typically offer lower spatial resolution for turbulence measurements and require more complex data interpretation. Thus, while both instruments have limitations in resolving flow turbulence, using ADVs and ADCPs together provides a more comprehensive understanding of turbulence across different flow conditions and depths. In addition, even though the flow in a river bend is fully three-dimensional, we chose to study the relationship between turbulence parameters and local conditions. Water-column height and ice conditions directly influence shear velocity, turbulence production, and the interaction between bed- and ice-generated turbulent layers, thereby affecting the turbulence measured at each drill hole.

In the ADCP data set, velocity fluctuations were greater in the streamwise (u) and cross-streamwise (v) components whereas the vertical component (w) varied less (Figure 4). In contrast, the ADV data revealed greater

Table 3
Calculated Turbulence Parameters by Measurement Device and Measurement Year

Data set	Parameters
ADCP 2016-2024	TKE_{min}, τ_{uw}, τ_{vw}
ADV 2020-2024	τ_{uv}, TI_u, TI_v
ADV 2020, 2021, 2024	TKE, τ_{uw}, τ_{vw}, TI_w

Note. Spearman correlation analyses were conducted for the complete ADCP and ADV data sets as well as individual data sets described in the table.

fluctuations in the vertical component in the upstream. This discrepancy may result from instrument differences (Nystrom et al., 2007) or local turbulence conditions influenced by riverbed topography and water column height. Therefore, the ADV and ADCP data sets are not directly comparable. The ADV measurements provide higher-quality information on near-bed flow characteristics whereas ADCP is more prone to measurement bias caused by sidelobe interference. Conversely, the ADCP data set offers a longer-term perspective, allowing analysis of how varying hydrological conditions over the studied 9 years influence the calculated parameters. Overall, velocity conditions in the upstream section exhibit greater variability across all components whereas flow in the downstream is more stable.

3.5. Data Processing and Plotting

3.5.1. Filtering of the ADV Data

To account for measurement errors in the ADV data, we follow the filtering procedure Wilcox and Wohl (2006) presented, with some modifications due to our study site and aims. The procedure comprises five steps, and the filtered data resulting from the previous step is always used as the input for the following step. First, we remove from consideration any momentary measurements with signal-to-noise ratios (SNRs) below 2 dB or above 35 dB. The water in Pulmanki River is very clear during winter, with hardly any suspended sediment, and as such, the SNR values are typically very low. We therefore opt to include data with SNR values between 2 and 35 dB. According to the measurement device's manufacturer (SonTek, 2019), it can measure velocities down to 2–3 dB. In addition, we controlled the differences in the mean magnitudes of the velocity components between momentary

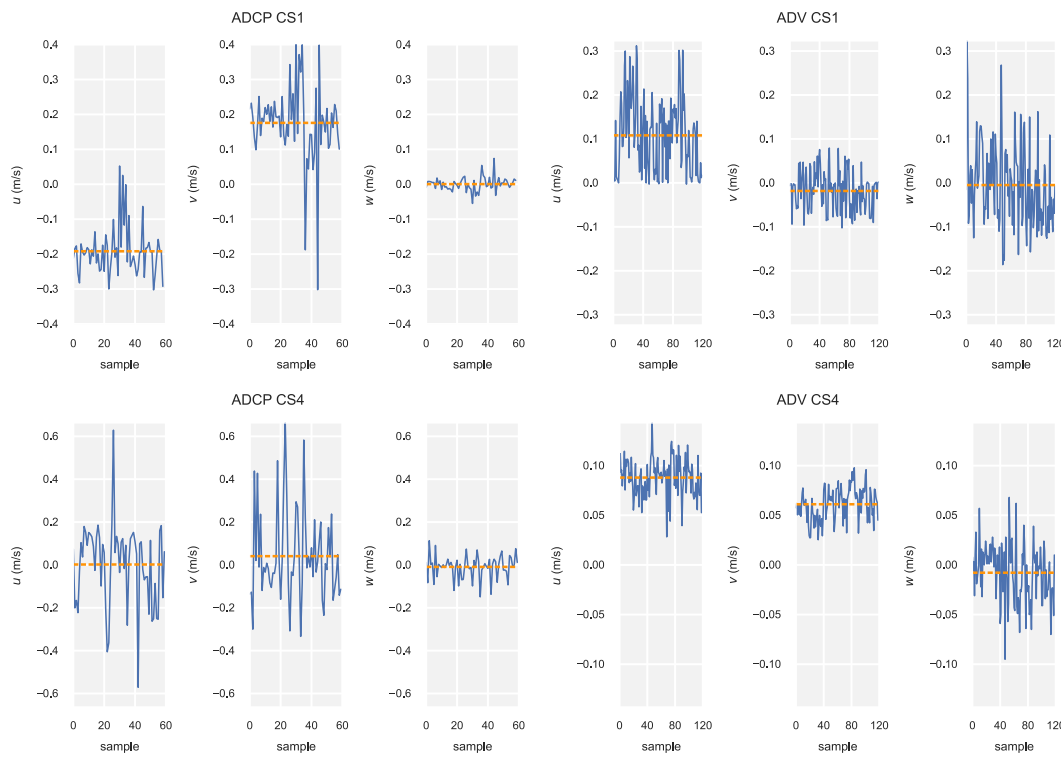

Figure 4. Example of the velocity fluctuations in u, v, and w components from ADCP and ADV observations from 2024 in upstream (CS1) and downstream (CS4) locations. In the example, ADV and ADCP measurements from one drill hole from CS1 and CS4 are compared. The blue line indicates momentary velocity component values, and the orange dashed line indicates the mean of the values, calculated from the momentary component values. Note the different scales on the velocity component axes. Each sample corresponds to one second of measurement, and the mean values are used in the turbulence parameter calculations.

measurements that had SNR values of below and above 10 dB. This is the threshold recommended by the device manufacturer for good measurements (SonTek, 2019). The differences were below or within one order of magnitude in nearly 90% of the averaged velocity components. Hence, we utilized the aforementioned limit of 2 dB. Due to the low turbidity of the water at the measurement site during wintertime, this first filtering step removes a great amount of data.

Second, we perform a so-called de-spiking procedure, in which we remove any momentary values, u, v, w, where the standard deviation with respect to the time average exceeds 3, as in Wilcox and Wohl (2006). However, because turbulence is fundamentally three-dimensional in nature, we do not utilize the fact the velocities along the vertical axis ($v_3 = w$) are decoupled from the velocities in the horizontal plane (v_1, v_2, u, v), as in Wilcox and Wohl (2006). Instead, if any of the momentary values, u, v, w, exceeds the standard deviation threshold, we reject the entire momentary measurement. Possibly because the first filtering step is so effective, de-spiking removed almost no further measurements.

Third, to maintain sufficient data for time averaging, we reject any 50-, 60-, or 120-s time series in which more than half of the momentary measurements have been removed above. Now, because we have a mix of two-dimensional and three-dimensional ADV data, we cannot meaningfully use the normalized root mean square velocity criteria Wilcox and Wohl (2006) employed, so as the final filtering step, we test for any time series in which the standard deviation of any of the SNR channels equals zero, again as in Wilcox and Wohl (2006). Note that we omit the final step (i.e., manual data removal, presented in Wilcox and Wohl (2006)) because the previous steps filter data effectively, making the last step unnecessary in our case. As a result of the full filtering procedure, a fraction of the ADV time series is completely excluded from the analysis whereas some of the remaining time series are partially shortened.

3.5.2. Pre-Processing and Filtering of the ADCP Data

To filter the momentary ADCP data, we follow a procedure mostly like the one employed with the ADV data. However, before filtering, we pre-process the ADCP data to only obtain reliable near-bed values. First, we only include drill holes where the lowest measured depth was within 25 cm of the riverbed to account for the blanking distance (5 cm) and velocity profiling limitations (20 cm) specified by the device manufacturer (SonTek, 2022). This is done to remove cases in which the ADCP device cannot measure velocities close enough to the riverbed for them to be considered near-bed velocities. If valid data are available in the lowest 25 cm of the water column, the measurement cell closest to the riverbed is selected as the near-bed value.

Second, when looking at near-bed velocities only, we remove any measurements from drill hole locations where all the near-bed velocity components are exactly zero because these values likely result from instrument malfunction. Third, following the ADV filtering approach, we discard any drill holes that contain less than half of the expected number of momentary measurements. Although this may occasionally result from a short recorded timeseries, it is most often a consequence of the second filtering step mentioned above. We then apply the same filtering process as described above for the ADV, except we do not establish an upper limit for the SNR values in ADCP data because high and consistent SNR values are not generally considered measurement errors in the case of ADCP measurements whereas manufacturers have recommendations for low SNR values (SonTek, 2022). For the ADCP data, filtering effects were minor, with most removals occurring during pre-processing.

3.5.3. Accounting for Plot Limitations

The shear stresses and turbulence intensities resulting from our calculations can vary over several orders of magnitude, making effective visualization challenging. We perform a simple outlier removal for these data outputs to mitigate this. In our method, we remove from our plots shear stress and turbulence intensity data points that are over one order of magnitude larger than the corresponding median of each data set (per year and cross-section). Because the values are often very tightly clustered around zero, this is performed with the exception that if the absolute value of the median is smaller than 2.0 Pa in the case of shear stress data and 2.0 in the case of unitless turbulence intensity data, the true median is replaced with this comparison value. These filtered data sets were used only for figures; all statistical analyses were conducted using the full, unfiltered data.

Table 4
Summary of Winter Climate and Ice Cover Characteristics During the Observation Period (2016–2024)

Measurement date	Stable ice cover formation date	Min temp before measurement date (°C)	First below 0°C mean temperature date	Thaw days since first below 0°C mean temp. Date	Thermal winter start date	Thaw days since thermal winter start date	Frost sum before measurement date (excl. Thaw days)	Frost sum before measurement date (incl. Thaw days)
16.02.2016	14.12.2015	−38.1	4.10.2015	24	23.10.2015	12	−1,019.2	−1,001.8
16.02.2017	28.12.2016	−38.7	17.10.2016	22	1.11.2016	10	−783.6	−772.7
09.02.2018	23.11.2017	−35.2	19.10.2017	9	22.10.2017	8	−1,125.8	−1,119.4
07.02.2019	25.12.2018	−35.6	29.9.2018	36	19.10.2018	22	−873.6	−829.6
05.02.2020	3.1.2020	−38.5	4.10.2019	10	12.10.2019	4	−1,004.8	−1,003.8
15.02.2021	3.12.2020	−32.4	27.9.2020	43	16.10.2020	24	−833.8	−794.7
21.02.2022	28.10.2021	−31	18.10.2021	8	18.10.2021	8	−1,223.3	−1,211.7
21.02.2023	21.11.2022	−31	30.9.2022	35	20.10.2022	15	−848.4	−827.6
16.02.2024	26.11.2023	−34	7.10.2023	10	7.10.2023	10	−1,391.6	−1,379.5

Note. Freeze-thaw indicators are calculated based on the FMI's Nuorgam weather station data (Finnish Meteorological Institute, 2025). Stable ice cover formation date was based on time-lapse camera pictures taken upstream of the studied meander bend.

3.6. Statistical Analyses of Turbulence Parameters

Statistical analyses were conducted using Spearman's correlation coefficient, chosen due to the non-normal data distribution. Correlation coefficients and p-values were calculated to assess the strength and significance ($p < 0.05$) of the relationships between turbulence parameters and hydrological variables, such as water column height and ice thickness. Analyses were applied to the complete ADCP and ADV time series and, when possible, separately for annual and cross-sectional data sets. Annual analyses comprised all calculated values considered by year whereas cross-sectional analyses comprised all values by cross-section. Annual and cross-sectional analyses based on fewer than 15 samples were excluded from the results.

4. Results and Discussion

4.1. Hydroclimatic Controls and Spatial Variability of Flow Conditions Beneath Ice Cover at the Study Site

Across years, minimum measured air temperatures prior to field campaigns ranged from −31°C to −38.7°C, indicating that winter conditions at the study site are consistently harsh (Table 4). Winters were differentiated by their duration and thaw periods, which were compared using frost sums and the number of freezing degree days. The cumulative frost sums, excluding thaw days, varied from −783.6 in 2017 to −1391.6 in 2024 (Table 4). Including thaw days reduced the absolute frost sums slightly. Notably, 2018 and 2022 also exhibited very high frost sums, reflecting cold and sustained winters, whereas 2019, 2021, and 2023 represented milder conditions. Years 2016 and 2020 represented relatively similar conditions, which were average compared to the other years.

The first daily mean temperature below 0°C typically occurred between late September and late October, but the number of subsequent thaw days varied substantially and strongly influenced ice-formation timing. Years with short transitions, such as 2018 and 2022, produced early ice cover whereas extended thaws in 2019, 2021, and 2023 delayed freeze-up until December or even January. Similarly, the onset of thermal winter varied from early October to early November, but its effect on ice formation was mediated by the frequency of thaws after onset. As a result, stable ice cover formation dates varied by more than 2 months, from late October to early January. Severe winters with large frost sums tended to support thicker ice, though the relationship is not linear, highlighting the additional influence of annual hydroclimatic conditions at the study site.

Discharges were lowest in 2018 and 2024, coinciding with strong frost sums, whereas weaker frost sums in 2016 and 2017 were accompanied by higher discharges. In 2016 and 2017, the number of thaw days following the first below 0°C mean temperature was also relatively high. Later ice cover formation, as in 2016 and 2020, coincided with higher discharges, whereas early ice cover formation, as in 2018 and 2022, corresponded to lower flows.

10.1029/2025WR042447

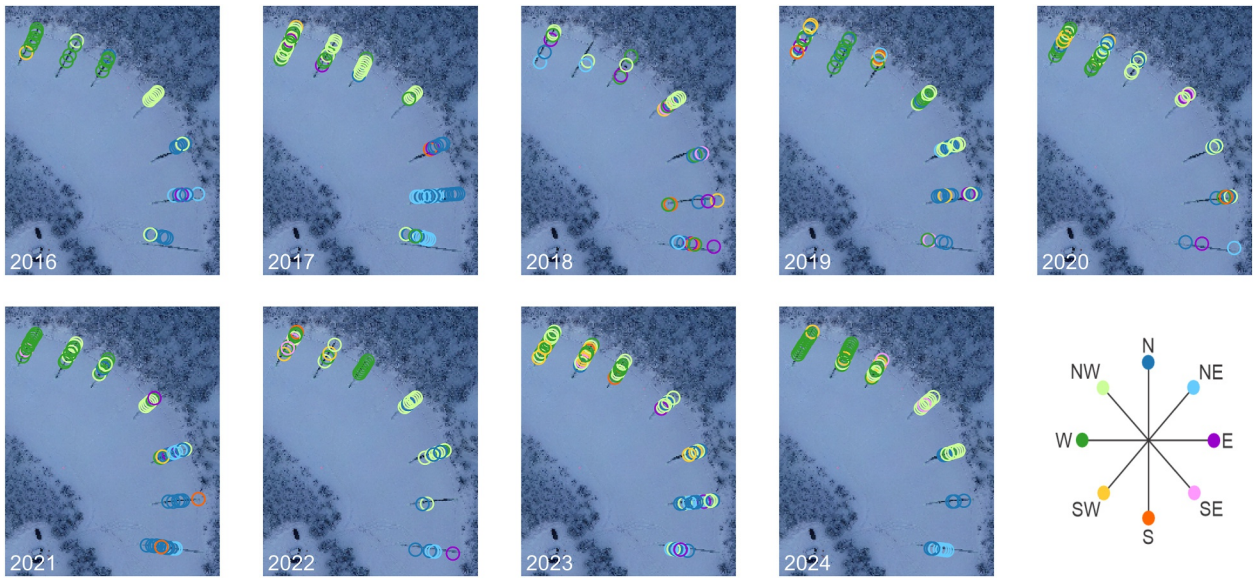

Figure 5. Near-bed flow directions in the study site from 2016 to 2024 during various discharge and ice cover conditions. The main direction of the near-bed flow is between west and north.

However, relationships among discharge, ice cover formation, and weather variables cannot be confirmed statistically given the 9-year data set, underscoring the need for longer time series.

During ice-covered conditions, variability in all velocity components was generally greater in the upstream cross-sections than in the downstream ones, regardless of ice thickness. This pattern is attributed to the shallower channel depth upstream, which leads to higher flow velocities and consequently more turbulent flow conditions (Sukhodolov, 2012). Data from ADCP and ADV measurements support these observations. However, as in the open-channel season (Salmela et al., 2020), velocities in the downstream part of the studied meander bend increased as water exited the pool at the apex and moved toward the riffle below the bend.

Near-bed flow directions (in geographic degrees) used for further analysis were derived from the ADCP data set; turbulence metrics from the ADCP and ADV are treated in later chapters. In the study area, near-bed flow directions align (Figure 5) with the primary flow direction in the bend although secondary flow structures are also evident in the flow direction data (Figure 6). Variations in the position of the high-velocity core and the two helical flow cells near the meander apex were observed in the complete water column data when the total discharge and the height of the water column beneath the ice cover were sufficient to allow for their formation (Figures 7 and 8). These observations are consistent with the findings of Lotsari et al. (2017) from the same study area. Because centrifugal acceleration is more pronounced near the bed, it induces a helical rotation in the opposite direction (Demers et al., 2011), which is noted in the flow direction and speed patterns in the data. These secondary flow patterns, including helical rotation caused by near-bed centrifugal acceleration, were also evident throughout the entire water column by Lotsari et al. (2017).

4.2. Effects of Water Column Height Beneath Ice Cover on Near-Bed Turbulence

Water column height varied between measurement locations and years, but the variation was smaller than that observed for ice thickness and discharge. The maximum water column height was 1.47 m in 2019 whereas in 2016 and 2020, the maximum recorded height was only 0.8 m (Table 1). The minimum water column height was generally around 0.2 m; however, shallower areas could not be drilled to avoid damaging the ice auger due to the high sediment content in the ice. The influence of water column height on near-bed turbulence was assessed using statistical correlations between height and turbulence derived from the ADCP and ADV measurements. Overall, near-bed turbulence generally decreased as water column height increased: a shallower water column concentrated flow and shear stress near the bed, raising TKE and turbulence intensities. This relationship depended on discharge, being most evident at moderate to high flows and weaker in low-flow years.

10.1029/2025WR042447

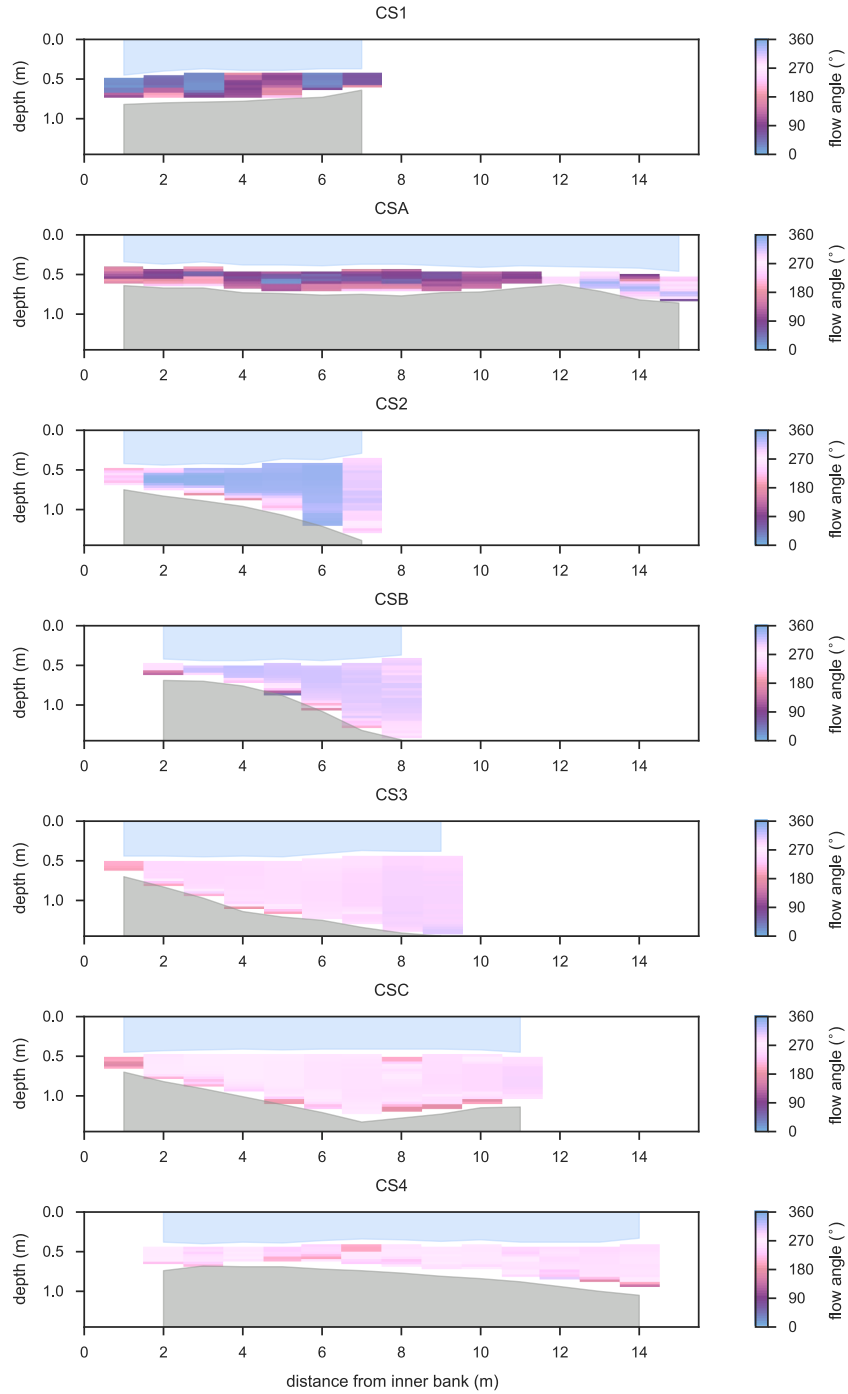

Figure 6. Flow directions across cross-sections based on ADCP measurements in the study site for 2023, selected as the year most representative of the overall hydrological conditions and with the most complete data.

In the results of the statistical analysis of the complete ADCP data set (Table 5), a moderate negative correlation was observed for the TKE_{min}. This suggests that TKE_{min} decreases as the height of the water column above the bed increases. In cross-section-wide analysis (Appendix A), a similar statistically significant negative trend was present mid-bend and downstream of the study site (CS2, CSC, and CS4) in areas where near-bed flow velocities were observed to be slower (Figure 9). When correlation analysis was conducted for each year individually (Appendix A), the trend of TKE_{min} decreasing with the increase of water column height was present for all years

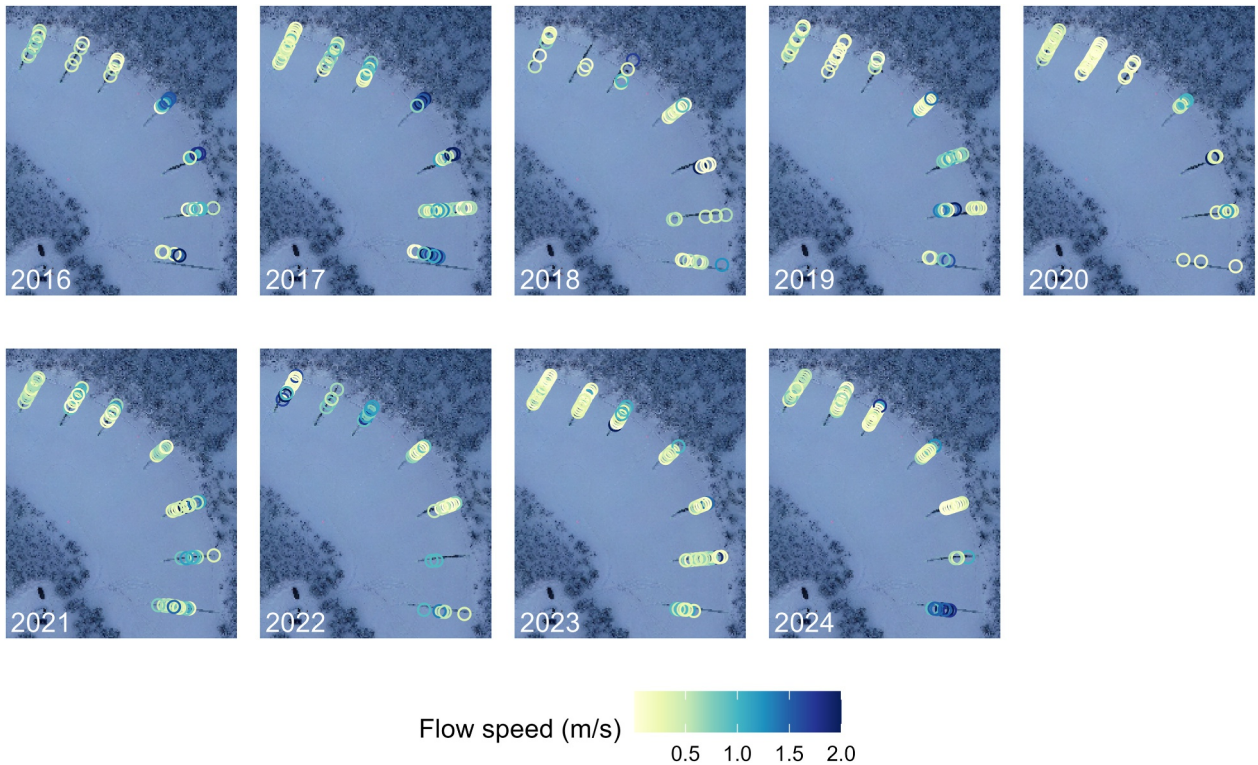

Figure 7. Annual average near-bed flow speeds measured in each drill hole with ADCP. The greatest near-bed flow speeds are typically measured in the upstream and the apex of the studied bend.

except 2018 and 2020 (Figure 10). Notably, these 2 years corresponded to the lowest discharges in the data set (0.18 and 0.79 m^3/s, respectively), suggesting that under low-flow conditions, the water column height's influence on near-bed turbulence may be diminished or masked by reduced energy input into the system (Lotsari et al., 2022). At the same time, the shallowest mean water column heights (0.34 and 0.42 m, with maximum depths of 0.87 and 0.80 m) were observed, indicating that turbulence generation in the near-bed region was likely suppressed overall, which may explain why the expected negative correlation with water column height was not evident in these years.

A weak but statistically significant negative correlation between τ_{uw} and water column height was observed in the full ADCP data set. This correlation was not present in all years; however, it was strongest in 2016 and 2023, which had different discharge levels (1.38 and 0.99 m^3/s) but both showed consistent negative correlations (Appendix A). This suggests that the inverse relationship between water column height and shear stress may be consistent across a range of discharge conditions as increasing water column height raises the flow depth above the bed and weakens vertical momentum exchange. A similar but not statistically significant negative trend was observed in CSB and CS3 in the cross-section-wide analysis (Appendix A). These locations typically show the most distinct differences in water column height, with shallow inner-bend areas and deeper outer-bend areas (Figure 11).

The statistical analysis of ADCP and water column height data revealed that TKE_{min} tends to decrease when the water column height above the bed increases. Similarly, the shear stresses follow a similar trend in some cases in our study site. These findings may be a result of the ice cover deepening the location of maximum flow speed within the water column (Robert & Tran, 2012; Smith et al., 2023). When the water column between the bed and ice cover is shallow, the maximum flow speed likely occurs closer to the bed, exerting a greater influence on turbulence than in situations in which the space between the bed and the ice underside is wider. Our finding aligns with previous studies showing that turbulence parameters are greater when the water column between the riverbed and ice cover is shallow (Koyuncu & Le, 2022; Kumar et al., 2025). Kumar et al. (2025) observed that TKE and shear stresses are highest near the bed and sidewalls of a sand-bed flume and that bed roughness enhances the

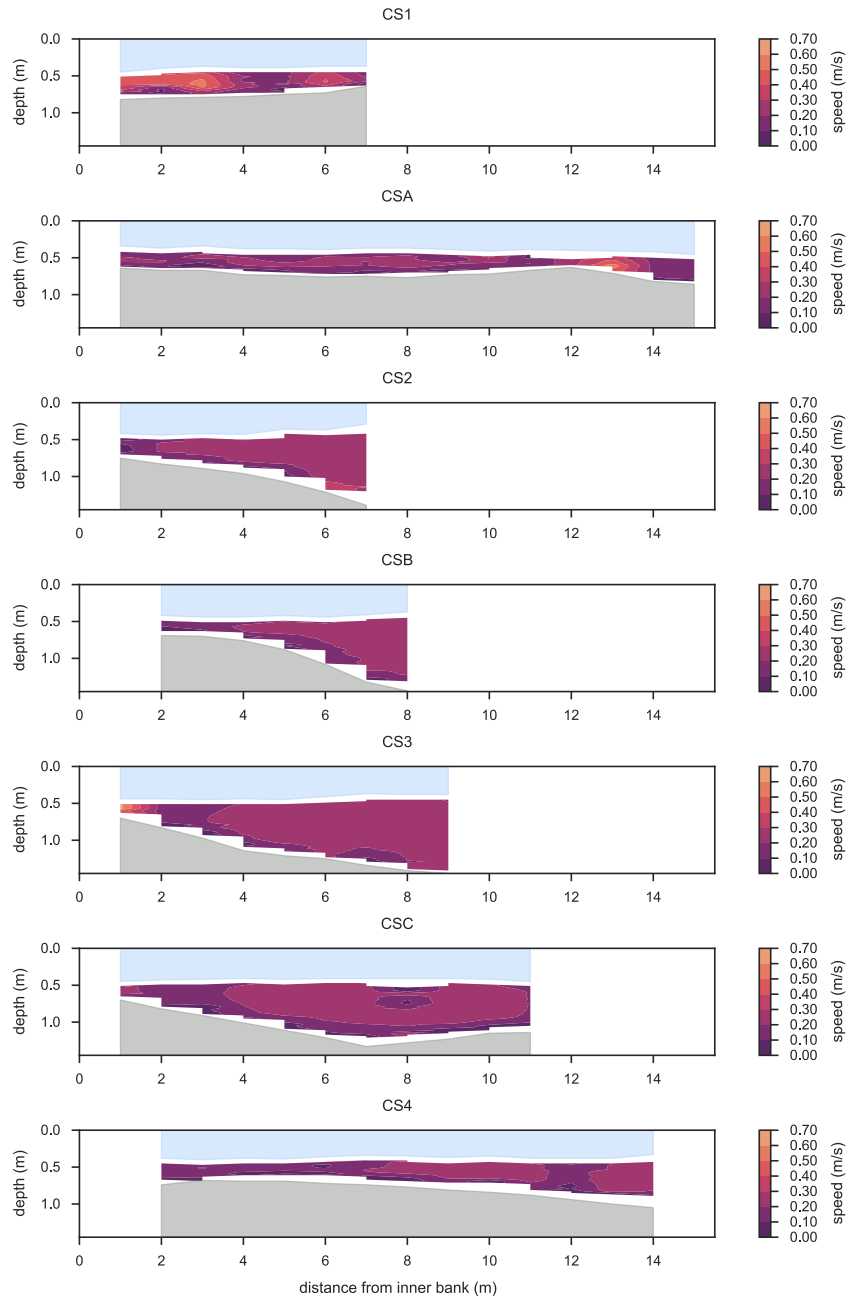

Figure 8. Average flow speeds across cross-sections in 2023. The sample year 2023 illustrates variations in the position of the high-velocity core and the development of two helical flow cells (CS1, CSC and CS4), which form when discharge and water column height below the ice cover are sufficient.

small-scale turbulence in the near-bed region of an open channel. Koyuncu and Le (2022) found that ice cover significantly alters the velocity profile, especially near the banks, where the water column is shallower, and influences sediment transport processes. In these near-bank areas, they observed shear velocities comparable to those measured high-discharge open-channel conditions. Studies of open-channel conditions have also shown that TKE values are higher near the bed and decrease with height in the water column, suggesting more intense turbulence in the near-bed region (Behera et al., 2023; Sukhodolov, 2012).

Overall, the water column height's influence on near-bed turbulence seems influenced by discharge volume as well. The negative correlation with TKE_{min} present in the ADCP data seems to hold more consistently during

Table 5
Correlation Between Water Column Height and Turbulence Variables of the Complete Data Set, Including Calculated Variables From all Measurements From All Years

Variable	n	Correlation	Sig. (p-value < 0.05)
ADCP data set			
τ_{uw}	470	**−0.1**	**0.034**
τ_{vw}	470	0.05	0.23
TKE_{min}	470	**−0.57**	**0.00**
ADV data set			
τ_{uw}	75	0.11	0.34
τ_{vw}	75	−0.16	0.89
τ_{uv}	197	−0.07	0.34
TKE	75	−0.04	0.56
TI_u	197	**−0.20**	**0.004**
TI_v	197	0.04	0.6
TI_w	75	**0.23**	**0.04**

Note. Bold values denote statistically significant (p-value < 0.05) correlations.

moderate to high flow conditions. In low-flow years, such as 2018, the correlation between water column height and near-bed turbulence weakens, likely due to reduced flow energy and flatter velocity profiles. This suggests that near-bed turbulence under ice cover is influenced not just by water column height but also by how flow velocity is distributed through the depth. In addition, this suggests that hydrological conditions prior to freezing, which affect discharge volume, play a role in controlling turbulence. The conditions prior freeze-up (e.g., low or high water level) partly determine the water column height beneath the ice cover and, together with flow conditions at the time of freezing, subsequently contribute to turbulence formation. These findings show that near-bed turbulence has interannual variability, which covaries with water column height and discharge.

The ADV results (Table 5) provided more detailed insights into the effects of water column height than the ADCP ones, for a broader range of turbulence variables could be derived from the data set. For the complete time series, a statistically significant negative correlation was found for turbulence intensity in the streamwise direction (TI_u), and a significant positive correlation was observed for vertical turbulence intensity (TI_w). No significant correlations were found for other turbulence parameters.

In the annual analysis of the ADV data set, a significant negative correlation between TI_u and water column height was observed in 2022 (Appendix A). TKE showed a negative but non-significant correlation in 2020 and 2024 whereas TI_w had a significant positive correlation in 2024. Shear stress components and turbulence variables generally showed weak or non-significant correlations across all years. On cross-section-wise analysis, a significant negative correlation between water column height and TI_u was observed in CSA, CS2, and CS3. A positive significant correlation was also observed between τ_{uv} and CS2. The decrease in TI_u with increasing water column height (Figure 12), accompanied by an increase in TI_w, can be explained by water column height: greater height provides more vertical space for larger eddies that enhance TI_w whereas increasing elevation above the bed reduces turbulence intensities (Muste et al., 2000). This phenomenon was observed both in the full ADV data set as well as in the cross-sectional analyses.

TKE was analyzed using two approaches due to differences in the measurement methods of the two applied devices. From the ADCP data, turbulent kinetic energy was derived as a lower-bound estimate of TKE_{min}, which represents the minimum possible value of TKE, and from the ADV data as the full measure of TKE. Research has shown that in a meander bend under ice cover, flow speeds throughout the entire water column decrease with increasing depth; this pattern is typical for the downstream part of an apex (Lotsari et al., 2017). This trend was particularly evident in the deeper sections of the cross-sections, where near-bed flow speeds were lower than those near the inner bank. Regarding TKE_{min} values, this suggests that TKE_{min} is higher in areas with a shallower water column between ice and riverbed, as observed in our measurements. As the water column height increases beneath ice cover, the location of maximum flow moves toward the surface, reducing flow speeds in the near-bed region. This aligns with the observation by Koyuncu and Le (2022) that under ice-covered conditions, the maximum flow speed location is frequently closer to the ice layer, further supported by Attar and Li (2013), who found that if the riverbed is rougher than the ice underside, the maximum flow speeds shifted toward the ice. Similarly, Lotsari et al. (2017) found that shallow flow conditions under ice are affected by the frictional forces from the channel bed and ice underside, leading to flow disturbances throughout the water column and hindering helical flow development. Robert and Tran (2012) found that in a flume, adding ice cover increased TKE in the near-bed region whereas in an open channel, TKE decreased when the height above the bed increased. In our study, the distance of ADV measurement from the riverbed was constant across drill holes, and TKE showed no significant relationship with water column height, decreasing slightly in most years.

In some cases, such as that of τ_{uv} in 2021, shear stresses decreased with increasing water column height, particularly in shallower areas near the inner bank. Although this trend was not consistent across all years or stress components, it aligns with the findings of Koyuncu and Le (2022), who observed that ice cover contributes to an increase in shear stress in shallower areas near the banks. They also noted that under low discharge conditions,

10.1029/2025WR042447

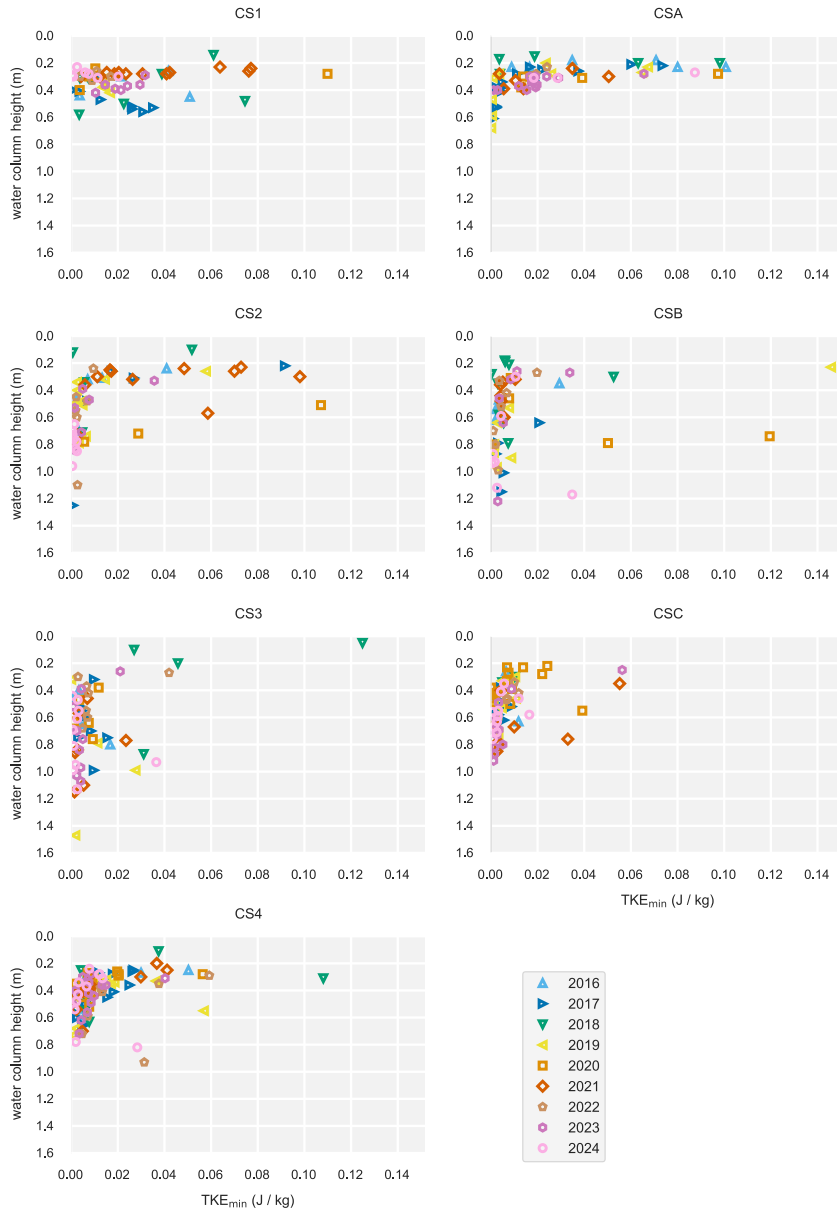

Figure 9. Relationship between TKE_{min} and water column height beneath ice cover across cross-sections from 2016 to 2024. Data points are color-coded by year.

shear stresses exhibited less variation than in high discharge flows, which aligns with our 2021 findings during relatively low discharge conditions.

4.3. Effects of Ice Thickness on Turbulence

Analyses of ADCP and ADV data sets showed that thicker ice cover was generally associated with reduced TKE_{min} but increased turbulence intensities in the streamwise and vertical directions. These effects were most evident during years with low discharge (<1 m^3/s), suggesting that ice cover's influence on turbulence is strongest under low-flow conditions. The results also indicate that ice cover can modify shear stresses and turbulence structures in ways that vary across cross-sections and years, reflecting the combined effects of ice formation, channel morphology, and hydrological conditions.

10.1029/2025WR042447

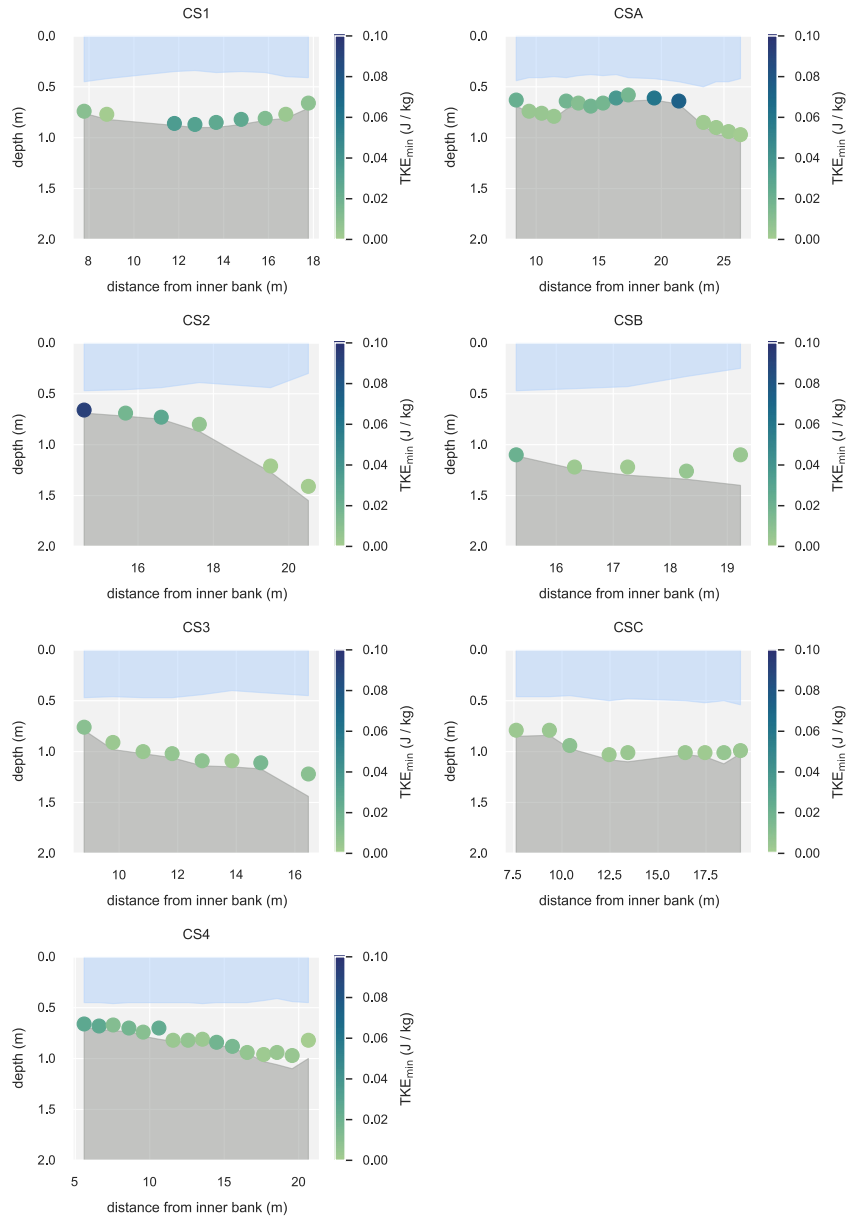

Figure 10. Example of cross-sectional variation of near-bed TKE_{min} along the study reach in 2017. Data set shows a general decrease in TKE_{min} with increasing depth. This trend was present for all years except 2018 and 2020. The ice cover is depicted in blue and the riverbed in dark gray.

During the study period, average ice thickness ranged from 0.35 m in 2019 to 0.58 m in 2022, with a maximum of 0.68 m in 2022 and a minimum of 0.15 m in 2018. No consistent relationship with discharge was observed (Table 1). Ice cover was typically thickest along the inner bend and thinner along the faster-flowing outer bend. The influence of ice cover thickness on near-bed turbulence was analyzed using the same methodology as applied for water column height. In the complete ADCP data set (Table 6), no statistically significant correlations were found for τ_{uw} or τ_{vw}. However, a weak but statistically significant correlation was observed for TKE_{min} indicating that near-bed turbulence levels decrease as ice cover thickness increases. Although in annual analyses statistically significant negative trend results were not present, borderline significance was observed in 2024 and 2021 (Appendix B), suggesting that this relationship may become more pronounced under certain seasonal conditions (i.e., discharge or ice cover conditions). Similarly, near-significant correlations between shear stress and ice cover thickness were found for τ_{uw} in 2016 ($p = 0.083$) and τ_{vw} in CS3 ($p = 0.1$). Typically, across all years, the thickest

10.1029/2025WR042447

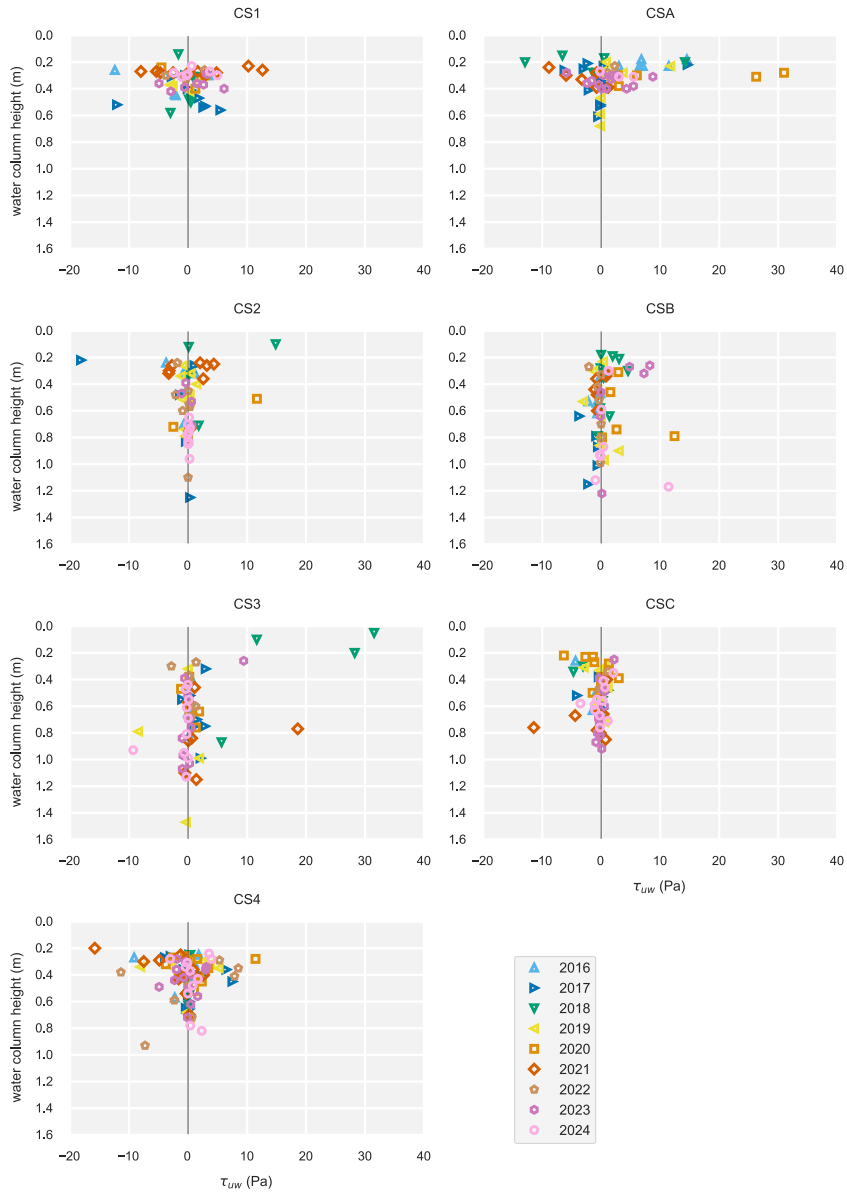

Figure 11. Streamwise-upwards shear stress τ_{uw} with respect towater column height across cross-sections. Data points are color-coded by year.

ice cover was observed in the inner bend, with thinner ice toward the outer bend. This pattern is characteristic of meander bends, where the inner bend is shallower and typically exhibits slower flow speeds, which facilitate greater ice accumulation. In contrast, the outer bend experiences faster flow conditions that restrict the ice thickening process.

The ADV data provided additional insights into the turbulence parameters. The results from the complete data set (Table 6) revealed a significant positive correlation for turbulence intensity in the streamwise (TI_u) and vertical (TI_w) directions and a significant positive correlation for the cross-stream–upwards shear stress (τ_{vw}). TI_u and TI_w had a moderate positive correlation. This suggests that streamwise (Figure 13) and vertical turbulence intensities increase when thicker ice cover is observed. Other turbulence variables showed weak and non-significant correlations with ice thickness.

10.1029/2025WR042447

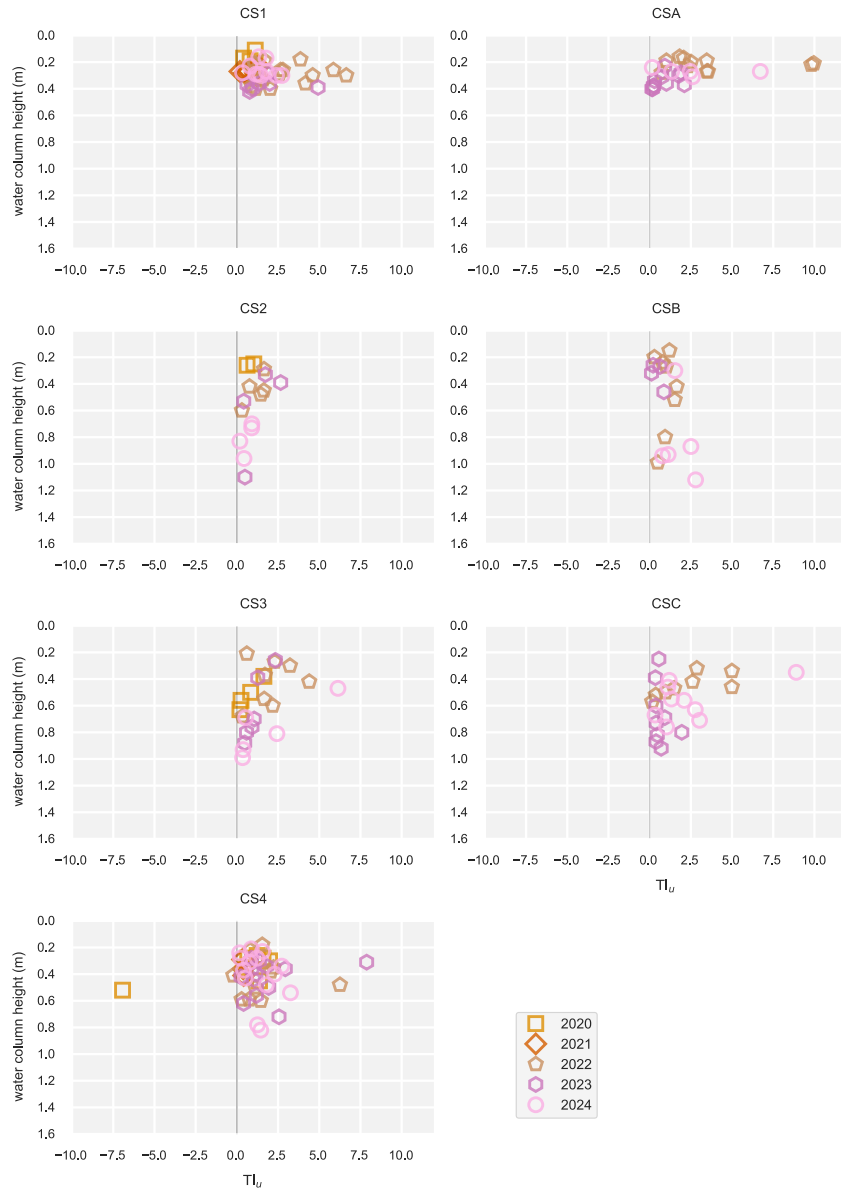

Figure 12. Streamwise turbulence intensity, TI_u, and water column height across cross-sections. In the statistical analysis, a negative correlation between water column height and TI_u was observed in cross-sections CSA, CS2, and CS3 (Appendix A). Data points are color-coded by year.

Annual analyses of the ADV data further support these findings. In 2021 and 2024 (Figure 14), TI_w exhibited a significant positive correlation with ice thickness, indicating that thicker ice cover enhances vertical turbulence in those years. In 2021, a significant negative correlation was also observed between τ_{uv} and ice thickness, indicating a reduction of horizontal-vertical shear stress below thicker ice. TI_u showed a near-significant positive correlation in 2020 ($p = 0.055$) but varied in direction and strength across other years. In 2024, a negative correlation between ice thickness and TKE was observed. A similar negative relationship was present between ice thickness and TKE_{min} in the ADCP data set; however, it did not reach statistical significance, as the p-value was 0.055, indicating a trend toward significance. In the cross-sectional analysis, statistically significant relationships were observed between ice thickness and τ_{vw} in CS4, demonstrating a positive trend. Furthermore, positive trends were also prevalent between TI_u and ice thickness in CS1, CSA, CS3 and CSC.

Overall, the ADCP and ADV results indicate that thicker ice cover enhances turbulence intensity in the streamwise and vertical directions while also altering shear stress patterns under low-flow conditions (less than

Table 6
Correlation Between Ice Cover Thickness and Turbulence Variables of the Complete ADCP and ADV Data Sets

Variable	n	Correlation	p-value (sig <0.05)
ADCP			
τ_{uw}	470	−0.04	0.42
τ_{vw}	470	0.02	0.63
TKE_{min}	470	**−0.18**	**0.00**
ADV			
τ_{uw}	75	0.05	0.64
τ_{vw}	75	**0.27**	**0.02**
τ_{uv}	197	−0.01	0.86
TKE	75	−0.11	0.35
TI_u	197	**0.23**	**0.001**
TI_v	197	0.09	0.21
TI_w	75	**0.31**	**0.007**

Note. Bold values denote statistically significant (p-value < 0.05) correlations.

1 m^3/s). Research has shown that introducing an ice cover increases turbulence intensities in scour holes, especially in the streamwise and vertical directions, and that below ice-covered flow, higher shear stresses at the riverbed are generated (Jafari & Sui, 2021; Muste et al., 2000). The strongest and most consistent correlations, particularly for TI_u, TI_w, and τ_{uv}, were observed in 2021 and 2024, which were characterized by lower discharges (0.5 and 0.76 m^3/s, respectively). In contrast, high-discharge years, such as 2016 and 2017 (1.38 and 1.32 m^3/s, respectively), showed weaker or no significant relationships, suggesting that elevated flow conditions may reduce ice cover's relative influence on near-bed turbulence. This points to discharge affecting how ice cover affects near-bed turbulence. The results indicate that discharge acts as amplifying factor on turbulence during low and moderate winter flows whereas higher flows decrease it. The positive correlation of τ_{uv} and ice thickness in the ADV data set was not detected in the ADCP data set, which may be explained by the fact that τ_{uv} values derived from the ADV data cover only 3 years of the study period due to instrument limitations.

4.4. Connection Between Near-Bed Flow Turbulence and Riverbed Morphology in 2024

In winter 2024 bedforms in the study reach were primarily dunes (Table 7). Plane beds were observed along the outer bank at CS1, CSA (upstream), and CSB and CS3 (mid-bend). At CS2, the bed was a plane across the entire cross-section. The transport stage parameter, which expresses particle mobility relative to the critical stage for initiation of motion (Van Rijn, 1984), was calculated under ice cover at the study site by Lotsari et al. (2022). These dimensionless values ranged from 0 to 20, typically remaining below 5. Their sediment samples from 2020 to 2021 indicated a D_{50} value between 0.42 and 0.78 mm. These findings of bedforms during 2024 align with earlier studies from the site and Van Rijn's classification, where dunes are expected under such conditions (Dey, 2014). Although bedform data is only available for 2024, we can assume that the bedforms are generally quite similar from year to year even though some bedforms may have shifted due to the sediment transport processes and annual depth changes of the cross-sections. However, the absence of multi-year morphology data limits the assessment of interannual turbulence–bedform interactions, highlighting the need for continued bedform monitoring in future research.

Winter 2024 was the most severe of the study period, with a frost sum of −1,391.6, exceeding other years. Although its minimum air temperature (−34°C) was not the lowest on record, the season was marked by consistently cold conditions and very few thaw days (10), which allowed frost sums to accumulate. Stable ice cover formed on 26 November. Overall, early cooling, limited thaws, and persistent cold made 2024 the harshest and most sustained winter in the data set.

Turbulence parameters from 2024 ADCP and ADV data sets were analyzed with bedform observations by comparing visual data and calculated values. Turbulence was higher over dune beds and lower over plane beds, consistent with open-channel studies (Behera et al., 2023; Kumar et al., 2025). These patterns were most evident at CS1 and CSA, where dunes, high velocities, and shallow water columns beneath the ice cover were present. Downstream (CS2 and beyond), where the channel deepens and bed morphology is flatter, turbulence decreased. Similar patterns were observed in other years, though bedform information for those years is limited.

The highest turbulence values generally occurred in the upstream section and inner bend, especially in TKE and TKE_{min}, which provide a comprehensive measure of turbulence intensity and flow dynamics (Figure 15; Table 7). Our observation aligns with laboratory (Kumar et al., 2025) and field-based modeling (Smith et al., 2023) studies showing that in shallow, fast-flowing reaches with bedforms such as dunes and ripples, the conditions foster heightened turbulence and increased TKE values near the bed due to enhanced flow-bed interactions and energy dissipation. Kumar et al. (2025) studied three-dimensional turbulent flow characteristics over sand beds in a narrow open channel, and they found that riverbed roughness elements, such as dunes and ripples, play a key role in generating strong turbulent eddies, resulting in elevated TKE and shear stress variation, particularly in the shallow upstream channel sections. Similarly, Smith et al. (2023) found that in a shallow riffle-pool sequence,

10.1029/2025WR042447

Figure 13. Streamwise turbulence intensity, TI_u, and ice thickness across cross-sections. Each point represents an ADV measurement, color-coded by year.

turbulence distribution was shaped by ice cover and channel morphology, with elevated TKE and flow velocities near the bed in areas of greater bed roughness. Supporting these findings, Sukhodolov (2012) observed maximum turbulence intensity near areas of pronounced bedform roughness under ice-covered and open-water conditions in natural environments.

At CS2, where the water column height beneath the ice increases and flow speeds decrease, TKE and TKE_{min} values are lower throughout the studied years. This reduction likely promotes the development of a plane bed. This pattern supports laboratory and field findings showing that TKE and turbulence intensity are typically largest close to the bed and fall off with increasing water column height and smoother bed topography (Kumar et al., 2025; Lotsari et al., 2020) because deeper, less rough near-bed layers weaken bed-induced shear and eddies generated by bedforms. Field observations from the same study reach report reduced turbulence in deeper, flatter sections, emphasizing that lower near-bed velocity and diminished bed roughness suppress turbulence production and limit sediment entrainment (Lotsari et al., 2020). In the lower bend in 2024, CS3 featured dunes along the

10.1029/2025WR042447

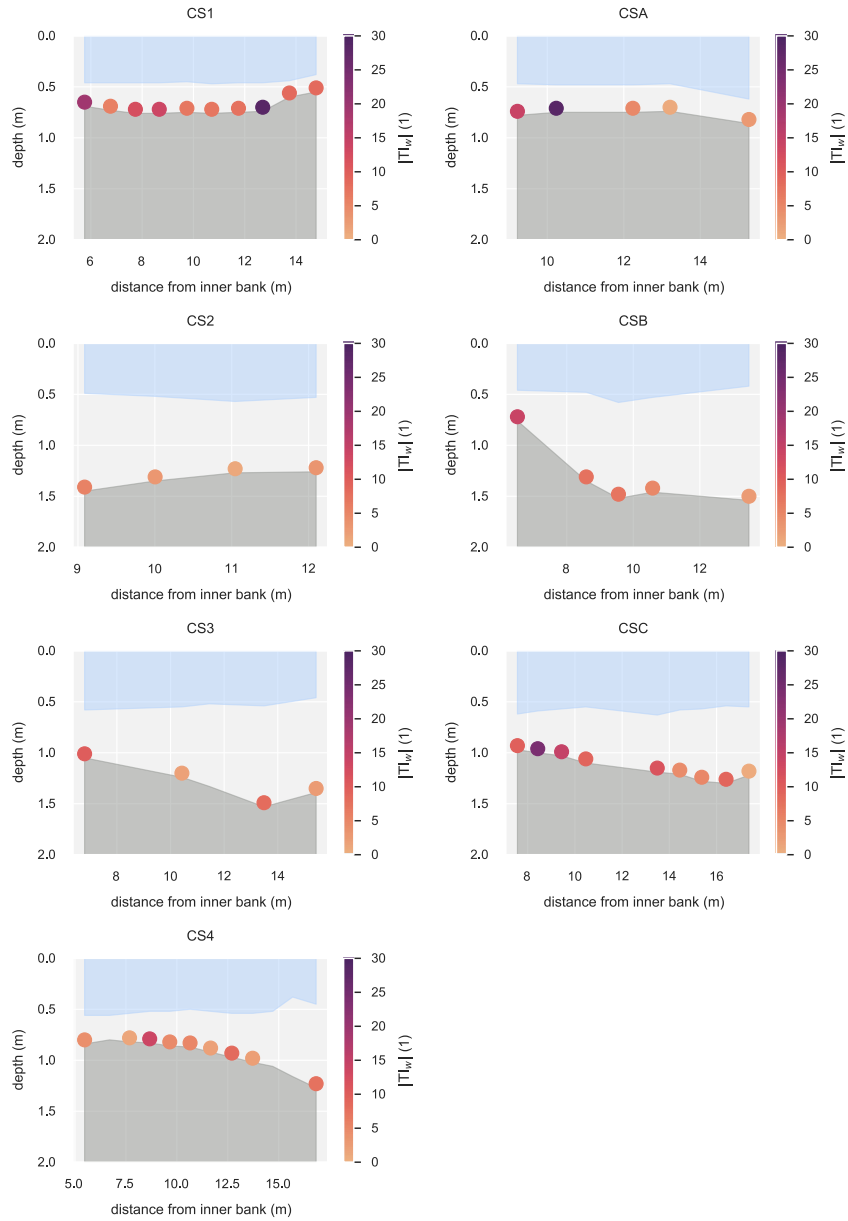

Figure 14. Spatial distribution of vertical turbulence intensity (TI_w) across cross-sections (2024), ADV measurements. The ice cover is depicted in blue and the riverbed in dark gray.

inner bend and plane areas on the outer bend whereas CSC and CS4 exhibited dunes across the entire section. Despite the presence of dunes, TKE values in the downstream cross-sections were elevated but less intense than upstream, likely due to increased water column height below ice cover, which reduces near-bed velocities and decreases turbulence (Kumar et al., 2025; Smith et al., 2023).

Shear stress values, particularly τ_{uw}, were also highest in CS1 and CSA, consistent with the flow acceleration at the inlet of meander bends. This aligns with Jamieson et al. (2010), who also observed elevated shear stress and turbulence levels in shallow, accelerating flows upstream of channel bends, often associated with the presence of active dune fields. These were present at the study site 2024. At CSB, τ_{vw} was elevated in 2024 in the drill hole closest to the point bar and in the drill hole where the channel geometry deepens from shallow to deep. This was likely due to the secondary flow and convergence effects at the apex of the bend. Jamieson et al. (2010) similarly demonstrated that secondary flows within river bends significantly increase transverse and vertical turbulence and

Table 7
Summary of Each Cross-Section's Riverbed Topography and Bedform Observations in 2024

Cross-section	Grain size	Bedform structure
CS1	Inner bank: Grains less than 2 mm, uniformly fine sand Outer bank: Sand, most grains 2–4 mm, occasional larger grains	Inner bank: dunes about 3–5 cm high, 10–15 cm long Outer bank: plane
CSA	Grains less than 2 mm, uniformly fine sand. Outermost drill hole: Clay streaks, fine sand, most grains under 2 mm, occasional larger grains	Inner bank: dunes about 3–5 cm high, 10–15 cm long. Outer bank: plane
CS2	Fine, most grains under 2 mm, occasional larger grains Outer bank: Clay streaks, fine, most grains under 2 mm, occasional larger grains	Plane
CSB	Inner drill hole: Grains less than 2 mm, uniformly fine sand Other areas: Clay streaks, fine sand, most grains under 2 mm, occasional larger grains	Inner bank: dunes about 3–5 cm high, 10–15 cm long. Outer bank: plane
CS3	Inner bank: Grains less than 2 mm, uniformly fine sand Outer bank: Clay streaks, fine sand, most grains under 2 mm, occasional larger grains	Inner bank: dunes about 3–5 cm high, 10–15 cm long. Outer bank: plane
CSC	Grains less than 2 mm, uniformly fine sand	Dunes about 3–5 cm high, 10–15 cm long
CS4	Grains less than 2 mm, uniformly fine sand	Dunes about 3–5 cm high, 10–15 cm long

shear stress components, particularly where channel curvature and bedforms interact. In general, higher shear stress values were associated with dunes whereas plane bed areas showed lower shear stress values, indicating that bedform roughness affects turbulence and shear stress across various river morphologies. Turbulence intensities were high in the upstream sections (CS1, CSA, and CS2), decreasing toward the downstream cross-sections as the flow transitioned into more stable conditions. In downstream locations (CS3, CSC, and CS4), TI and its variability was lower than in the upstream, reflecting the dissipation of energy and flow stabilization, matching with the observations of TKE and shear stress (Kumar et al., 2025; Simons & Richardson, 1966). Turbulence intensities were highest upstream (CS1, CSA, and CS2) and decreased toward the downstream as the flow transitioned into more stable conditions. In downstream locations (CS3, CSC, and CS4), TI and its variability was

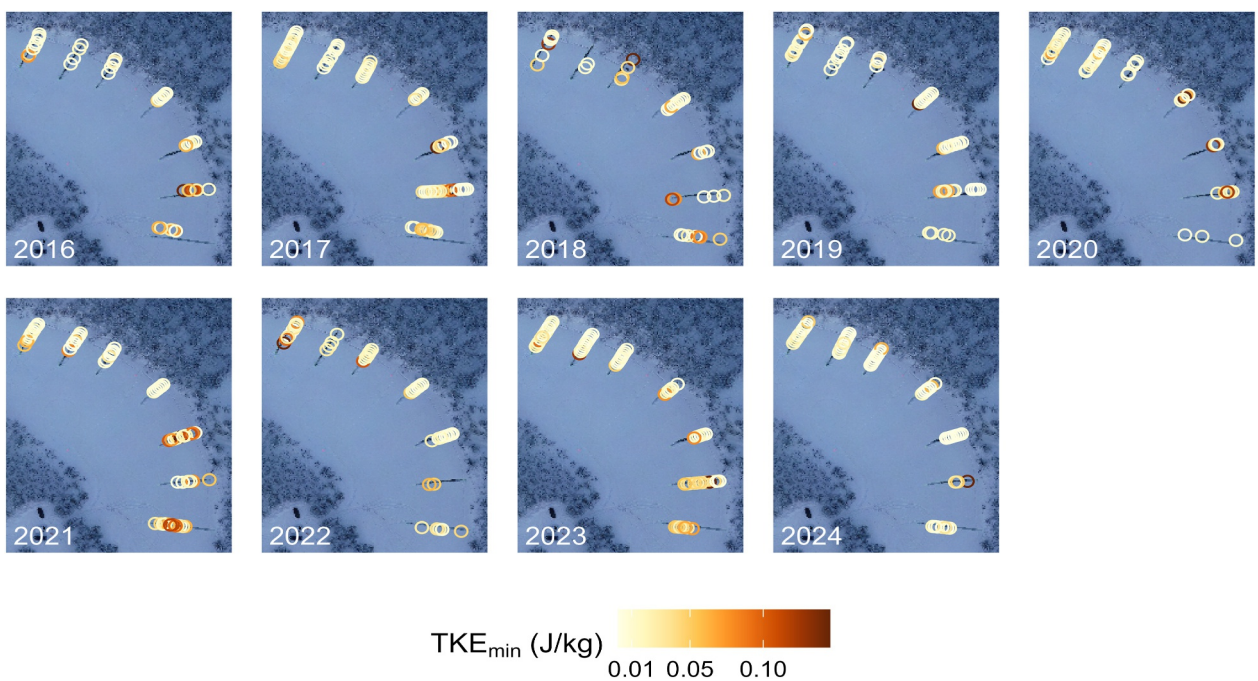

Figure 15. Calculated TKE_{min} values of each borehole in studied years.

lower than in the upstream, reflecting the dissipation of energy and flow stabilization, matching with the observations of TKE and shear stress.

Generally, the near-bed flow turbulence beneath river ice cover is weaker than in open-channel conditions, leading to decreased sediment entrainment, reduced sediment transport rates, and slower shifts in bedform dynamics (Turcotte et al., 2011). However, due to local variances in a meander bend, near-bed turbulence may intensify in areas such as riffles. This turbulence increase is observed where the water column beneath the ice is shallow and flow velocities are therefore high. As a result, sediment transport occurs at faster rates in these locations than in deeper sections, such as pools (Lotsari et al., 2022). The greatest impact of ice cover on flow occurs during its formation and melting phases, when the system transitions between an open and ice-covered channel. Similarly, sediment transport is most affected by ice cover during spring thaws (Ettema, 2008). Understanding these processes becomes more critical as we witness the shortening of ice-covered seasons and changes in ice cover thickness and breakup patterns. Observations from study sites in Northern Finland indicate that ice cover no longer forms as a single stable layer but instead undergoes repeated cycles of formation and melting in late autumn and early winter. These processes might affect turbulence and sediment transport and therefore require further investigation.

5. Conclusions

This study's results contribute to a better understanding of ice-covered river dynamics and provide insight into how the shortening or loss of seasonal ice cover may affect fluvial environments. The presence of ice cover alters flow conditions and promotes near-bed turbulence in shallow sections of meander bends by introducing an additional frictional boundary that shifts maximum velocities deeper into the flow and steepens velocity gradients toward the bed. Elevated turbulence and shear stress were observed in shallow upstream and inner-bend sections with dunes whereas deeper sections with flatter bed topography exhibited lower turbulence. Bedform roughness further increased near-bed turbulence and shear stress, with dunes generating stronger turbulence and intensified flow-bed interactions.

The results indicate that the height of the water column above the near-bed region has a greater influence on turbulence than ice thickness or winter severity. Water column height is not directly explained by the discharge volume during winter, but lower discharge beneath the ice was associated with reduced turbulence, reflecting diminished flow energy and flatter velocity profiles. Conversely, during years of elevated discharge, the influence of ice cover on turbulence was diminished, suggesting that higher discharge override the effects of ice. This also highlights discharge as a factor modulating how ice cover affects near-bed turbulence. Correlations between water column height and turbulence were strongest under moderate to high flow conditions and weakened during low-flow years. This suggests that pre-winter hydrological conditions, along with the timing and rate of freezing and freeze-thaw cycles, affect near-bed turbulence beneath ice cover. Ice thickness influenced turbulence in a more complex way: thicker ice tended to reduce overall turbulent kinetic energy but increased streamwise and vertical turbulence intensities. Thicker ice cover was also associated with larger frost sums and earlier freeze-up.

This study's results carry broader implications under changing climatic conditions. Shorter ice-covered periods, more frequent freeze-thaw events, and increasingly variable winter discharge regimes are likely to alter the spatial distribution of turbulence beneath ice cover, with consequences for channel morphodynamics and sediment transport. Further research is needed to clarify these interactions under varying flow and ice conditions, particularly during transitions from open to ice-covered channels, because near-bed turbulence controls sediment entrainment and transport and thus affects river channel morphodynamics.

Appendix A: Annual and Cross-Sectional Spearman Correlation Results of Water Column Height With Turbulence Metrics From ADCP and ADV Measurements

ADCP			
ANNUAL			
water column height ~ TKEmin	correlation	p-value	n
2016	**−0.644**	**0**	**39**
2017	**−0.548**	**0**	**69**
2018	−0.288	0.084	37
2019	**−0.509**	**0**	**53**
2020	−0.234	0.113	47
2021	**−0.717**	**0**	**62**
2022	**−0.607**	**0**	**42**
2023	**−0.771**	**0**	**66**
2024	**−0.422**	**0.001**	**57**
water column height ~ tau_uw	correlation	p-value	n
2016	**−0.383**	**0.016**	**39**
2017	0.117	0.339	69
2018	−0.253	0.132	37
2019	−0.234	0.092	53
2020	0.196	0.186	47
2021	0.095	0.462	62
2022	−0.155	0.327	42
2023	**−0.313**	**0.011**	**66**
2024	−0.186	0.167	57
water column height ~ tau_vw	correlation	p-value	n
2016	−0.201	0.22	39
2017	−0.034	0.785	69
2018	0.219	0.193	37
2019	0.192	0.169	53
2020	−0.019	0.897	47
2021	0.041	0.752	62
2022	0.161	0.307	42
2023	0.237	0.055	66
2024	−0.033	0.806	57
CROSS-SECTIONAL			
water column height ~ TKEmin	correlation	p-value	n
CS1	−0.134	0.31	59
CSA	**−0.647**	**0**	**66**
CS2	**−0.665**	**0**	**60**
CSB	**−0.457**	**0**	**59**
CS3	−0.196	0.137	59
CSC	**−0.508**	**0**	**72**
CS4	**−0.56**	**0**	**97**
water column height ~ tau_uw	correlation	p-value	n
CS1	0.016	0.906	59
CSA	−0.148	0.237	66

Appendix A
Continued

CS2	−0.051	0.701	60
CSB	−0.182	0.169	59
CS3	−0.199	0.13	59
CSC	−0.028	0.816	72
CS4	0.081	0.429	97
water column height ~ tau_vw	correlation	p-value	n
CS1	0.128	0.332	59
CSA	0.033	0.79	66
CS2	−0.065	0.624	60
CSB	0.103	0.436	59
CS3	0.09	0.497	59
CSC	−0.124	0.298	72
CS4	0.032	0.753	97
ADV			
ANNUAL			
water column height ~ tau_uw	correlation	p-value	n
2020	0.421	0.092	17
2021	0.161	0.636	11
2022			
2023			
2024	−0.085	0.572	47
water column height ~ tau_vw	correlation	p-value	n
2020	−0.135	0.605	17
2021	−0.078	0.819	11
2022			
2023			
2024	−0.064	0.668	47
water column height ~ tau_uv	correlation	p-value	n
2020	0.405	0.107	17
2021	**−0.676**	**0.022**	11
2022	−0.133	0.28	68
2023	−0.109	0.435	54
2024	−0.124	0.405	47
water column height ~ TKE	correlation	p-value	n
2020	−0.373	0.14	17
2021	0.166	0.627	11
2022			
2023			
2024	−0.078	0.601	47
water column height ~ TIu	correlation	p-value	n
2020	−0.273	0.29	17
2021	−0.363	0.272	11
2022	**−0.254**	**0.036**	68

Appendix A
Continued

2023	−0.205	0.137	54
2024	−0.083	0.577	47
water column height ~ TIv	correlation	p-value	n
2020	0.138	0.599	17
2021	**0.777**	**0.005**	11
2022	−0.205	0.137	68
2023	0.256	0.062	54
2024	0.043	0.776	47
water column height ~ TIw	correlation	p-value	n
2020	0.394	0.118	17
2021	0.129	0.706	11
2022			
2023			
2024	0.224	0.129	47
CROSS-SECTIONAL			
water column height ~ tau_uw	correlation	p-value	n
CS1	0.263	0.237	22
CSA	0.316	0.684	4
CS2	0.714	0.136	6
CSB	1	1	2
CS3	0.1	0.81	9
CSC	0.217	0.581	9
CS4	0.192	0.381	23
water column height ~ tau_vw	correlation	p-value	n
CS1	0.389	0.074	22
CSA	−0.316	0.684	4
CS2	0.029	1	6
CSB	−1.000	1.000	2
CS3	−0.017	0.982	9
CSC	0.250	0.521	9
CS4	−0.096	0.663	23
water column height ~ tau_uv	correlation	p-value	n
CS1	0.027	0.857	47
CSA	−0.085	0.681	26
CS2	**0.693**	**0.005**	**15**
CSB	0.009	0.976	14
CS3	0.208	0.338	23
CSC	0.223	0.274	26
CS4	−0.095	0.528	46
water column height ~ TKE	correlation	p-value	n
CS1	−0.011	0.960	22
CSA	0.316	0.684	4
CS2	−0.829	0.0058	6
CSB	−1	1	2
CS3	−0.383	0.313	9

Appendix A
Continued

CSC	−0.217	0.581	9
CS4	0.269	0.214	23
water column height ~ TIu	correlation	p-value	n
CS1	0.143	0.336	47
CSA	**−0.545**	**0.004**	**26**
CS2	**−0.600**	**0.02**	**15**
CSB	0.088	0.765	14
CS3	**−0.520**	**0.012**	**23**
CSC	**−0.348**	**0.082**	**26**
CS4	−0.039	0.796	46
water column height ~ TIv	correlation	p-value	n
CS1	0.05	0.739	47
CSA	0.215	0.291	26
CS2	0.039	0.893	15
CSB	**−0.594**	**0.025**	**14**
CS3	0.091	0.679	23
CSC	−0.360	0.071	26
CS4	−0.007	0.964	46
water column height ~ TIw	correlation	p-value	n
CS1	0.021	0.926	22
CSA	−0.316	0.684	4
CS2	0.543	0.297	6
CSB	1	1	2
CS3	−0.083	0.843	9
CSC	−0.617	0.089	9
CS4	0.071	0.746	23

Appendix B: Annual and Cross-Sectional Spearman Correlation Results of Ice Thickness With Turbulence Metrics From ADCP and ADV Measurements

ADCP			
ANNUAL			
ice thickness ~ TKE_min	correlation	p-value	n
2016	−0.034	0.836	39
2017	−0.196	0.106	69
2018	0.043	0.803	37
2019	0.043	0.759	53
2020	**−0.017**	**0.907**	**47**
2021	−0.222	0.083	62
2022	−0.032	0.840	42
2023	**−0.152**	**0.222**	**66**
2024	**−0.256**	**0.055**	**57**

Appendix B
Continued

ice thickness ~ tau_uw	correlation	p-value	n
2016	−0.281	0.083	39
2017	0.008	0.946	69
2018	0.189	0.261	37
2019	0.110	0.435	53
2020	−0.069	0.645	47
2021	0.007	0.958	62
2022	−0.022	0.891	42
2023	0.143	0.252	66
2024	−0.109	0.421	57
ice thickness ~ tau_vw	correlation	p-value	n
2016	0.069	0.677	39
2017	−0.028	0.819	69
2018	−0.118	0.488	37
2019	−0.162	0.248	53
2020	0.054	0.720	47
2021	0.032	0.805	62
2022	0.019	0.905	42
2023	−0.222	0.074	66
2024	0.244	0.068	57
CROSS-SECTIONAL			
ice thickness ~ TKEmin	correlation	p-value	n
CS1	**−0.113**	**0.396**	**59**
CSA	0.010	0.936	66
CS2	−0.176	0.179	60
CSB	−0.065	0.623	59
CS3	**−0.164**	**0.214**	**59**
CSC	−0.024	0.844	72
CS 4	0.038	0.708	97
ice thickness ~ tau_uw	correlation	p-value	n
CS1	**0.058**	**0.662**	**59**
CSA	−0.012	0.926	66
CS2	−0.157	0.232	60
CSB	−0.063	0.634	59
CS3	**−0.135**	**0.310**	**59**
CSC	0.091	0.447	72
CS4	0.024	0.814	97
ice thickness ~ tau_vw	correlation	p-value	n
CS1	**−0.048**	**0.719**	**59**
CSA	−0.090	0.472	66
CS2	−0.188	0.149	60
CSB	0.008	0.954	59
CS3	0.216	0.100	59
CSC	0.059	0.624	72
CS4	0.088	0.389	97

Appendix B
Continued

ADV			
ANNUAL			
ice thickness ~ tau_uw	correlation	p-value	n
2020	−0.402	0.110	17
2021	−0.447	0.168	11
2022			
2023			
2024	−0.088	0.55	47
ice thickness ~ tau_vw	correlation	p-value	n
2020	0.111	0.671	17
2021	0.251	0.456	11
2022			
2023			
2024	−0.007	0.964	47
ice thickness ~ tau_uv	correlation	p-value	n
2020	−0.197	0.448	17
2021	−0.612	0.045	11
2022	−0.108	0.383	68
2023	0.143	0.302	54
2024	−0.099	0.509	47
ice thickness ~ TKE	correlation	p-value	n
2020	0.273	0.289	17
2021	0.269	0.423	11
2022			
2023			
2024	**−0.294**	**0.045**	**47**
ice thickness ~ TIu	correlation	p-value	n
2020	0.473	0.055	17
2021	0.073	0.831	11
2022	−0.087	0.483	68
2023	−0.239	0.081	54
2024	−0.089	0.554	47
ice thickness ~ TIv	correlation	p-value	n
2020	0.177	0.496	17
2021	0.297	0.375	11
2022	0.014	0.910	68
2023	−0.077	0.582	54
2024	0.162	0.276	47
ice thickness ~ TIw	correlation	p-value	n
2020	0.027	0.917	17
2021	**0.690**	**0.019**	11
2022			
2023			
2024	**0.446**	**0.002**	47

Appendix B
Continued

CROSS-SECTIONAL			
ice thickness ~ tau_uw	correlation	p-value	n
CS1	0.143	0.524	22
CSA	−0.316	0.684	4
CS2	−0.029	1	6
CSB	1.000	1.000	2
CS3	−0.35	0.359	9
CSC	−0.160	0.682	9
CS4	−0.121	0.583	23
ice thickness ~ tau_vw	correlation	p-value	n
CS1	0.211	0.346	22
CSA	0.316	0.684	4
CS2	−0.029	1	6
CSB	−1.000	1.000	2
CS3	0.067	0.88	9
CSC	−0.655	0.055	9
CS4	**0.716**	**0.000**	**23**
ice thickness ~ tau_uv	correlation	p-value	n
CS1	−0.051	0.734	47
CSA	0.101	0.623	26
CS2	0.225	0.419	15
CSB	0.134	0.648	14
CS3	−0.197	0.367	23
CSC	−0.218	0.284	26
CS4	0.047	0.758	46
ice thickness ~ TKE	correlation	p-value	n
CS1	0.069	0.76	22
CSA	−0.316	0.684	4
CS2	−0.543	0.297	6
CSB	−1.000	1.000	2
CS3	0.183	0.644	9
CSC	0.176	0.650	9
CS4	−0.354	0.097	23
ice thickness ~ TIu	correlation	p-value	n
CS1	**0.390**	**0.007**	**47**
CSA	**0.423**	**0.028**	**26**
CS2	0.039	0.893	15
CSB	0.435	0.120	14
CS3	**0.562**	**0.005**	**23**
CSC	**0.495**	**0.01**	**26**
CS4	−0.024	0.875	46
ice thickness ~ TIv	correlation	p-value	n
CS1	0.134	0.368	47
CSA	−0.105	0.610	26
CS2	0.279	0.314	15

Appendix B
Continued

CSB	0.339	0.236	14
CS3	0.151	0.493	23
CSC	0.229	0.260	26
CS4	−0.074	0.623	46
ice thickness ~ TIw	correlation	p-value	n
CS1	−0.160	0.477	22
CSA	−0.316	0.684	4
CS2	0.829	0.058	6
CSB	1	1	2
CS3	0.417	0.270	9
CSC	−0.059	0.881	9
CS4	0.204	0.350	23

Abbreviationsand relevant quantities

ADCP	Acoustic Doppler Current Profiler
ADV	Acoustic Doppler Velocimeter
u	Streamwise velocity component
v	Cross-stream velocity component
w	Upwards velocity component
TKE	Turbulent kinetic energy
TKE_{min}	Lower-bound estimate of turbulent kinetic energy
TI	Turbulence intensity
TI_u , TI_v , TI_w	Component-specific turbulence intensities in the streamwise (u), cross-stream (v) and vertical (w) directions, normalized with the corresponding mean velocity components
τ	Reynolds stress tensor
τ_{uv}, τ_{uw}, τ_{vw}	Reynolds shear stress components in the streamwise–cross-stream (uv), streamwise–upwards (uw) and cross-stream–upwards (vw) planes
SNR	Signal-to-noise ratio
water column height	The distance between the underside of the ice cover and the riverbed

Conflict of Interest

The authors declare no conflicts of interest relevant to this study.

Availability Statement

The software Tucaco—Turbulence calculation code version 1.0.0 (Vilhonen, 2025), used for generating the turbulence quantities in Lintunen et al., 2025 as well as part of the manuscript figures, is preserved at https://doi.org/10.5281/zenodo.17867164, available via GNU General Public License v3.0, and is freely accessible also at https://gitlab.utu.fi/eevilh/tucaco-public. Calculated turbulence parameters, statistical analysis results, and corresponding code are preserved alongside near-bed flow values, water depth, and ice thickness data (Lintunen et al., 2025) and are available at https://doi.org/10.5281/zenodo.17984777.

Acknowledgments
We would like to thank Dr Maria Kämäri from the Finnish Environment Institute; MSc Franziska Wolff, MSc Mariana Verdonen, MSc Tiia Tarsa and MSc Marko Kärkkäinen from the University of Eastern Finland; William Speirs from the University of Queensland (Brisbane, Australia); Dr Carlos Gonzales-Inca and Dr Jouni Salmela from the University of Turku; Dr Nikita Tananaev from the Melnikov Permafrost Institute (Yakutsk, Russia); and MSc Juha-Matti Välimäki from Aalto University for their valuable fieldwork assistance between 2016 and 2024. The fieldwork would not have been possible without the drilling support provided by Tommi Andersson, Esa Karpoff, Jouni Lukkari, Otso Suominen and Ilkka Syvänperä from the Kevo Subarctic Research Institute of the University of Turku during 2016–2024. We also thank MSc Oona Oksanen and BSc Laura Kivirinne from the University of Turku for their assistance with data processing. This study is part of the PhD research project of MSc Lintunen, funded by the doctoral programme in Biology, Geography and Geology (BGG) of the University of Turku Graduate School (UTUGS). This research has been conducted with the support of Digital Waters Flagship (decision no. 359247; 359248), funded by the Research Council of Finland Flagship Programme. The ice-covered flow measurements were initiated under the post-doctoral research project of Dr Lotsari, funded by the Research Council of Finland (ExRIVER: Grant 267345). The work for this paper was also supported financially by other Research Council of Finland funded projects (DefrostingRivers: 338480, 346602, and 359917; HYDRO-RDI-Network: 337394 and 337279; AnthroCliMocs: 355018; International research mobility, to Finland from Russia, Dr. Nikita Tananaev: 333218). In addition, the work was funded by The European Union—NextGenerationEU Recovery instrument (RRF) through Research Council of Finland projects Green-Digi-Basin (347703; 347701) and HYDRO-RI-Platform (346161; 346167). Funding was received from the Maj and Tor Nessling Foundation (ExRIVER, Grants 201300067 and 201500046; Influence of river ice and fluvial processes on river environments now and in the future, Grant 201600042), Maa- ja vesitekniikan tuki ry (MVTT, "Changing northern rivers and their material transport under warming climatic conditions," Grant 43465), Emil Aaltonen Foundation ("kohdeapuraha" in 2016), and Strategic Research Council at the Academy of Finland (Competence-Based Growth Through Integrated Disruptive Technologies of 3D Digitalization, RobotiCS, Geospatial Information and Image Processing/Computing—Point Cloud Ecosystem, Grant 293389). The Department of Geographical and

References

Alho, P., & Mäkinen, J. (2010). Hydraulic parameter estimations of a 2D model validated with sedimentological findings in the point bar environment. *Hydrological Processes*, *24*(18), 2578–2593. https://doi.org/10.1002/hyp.7671

Attar, S., & Li, S. S. (2013). Momentum, energy and drag coefficients for ice-covered rivers. *River Research and Applications*, *29*(10), 1267–1276. https://doi.org/10.1002/rra.2611

Autio, J., & Heikkinen, O. (2002). The climate of northern Finland. *Fennia—International Journal of Geography*, *180*(1–2), 61–66.

Barahimi, M., & Sui, J. (2024). Flow structure and shear stress in the presence of both ice cover on water surface and leafless vegetation in channel bed. *Journal of Hydrodynamics*, *36*(2), 340–354. https://doi.org/10.1007/s42241-024-0021-y

Behera, P. K., Deshpande, V., & Kumar, B. (2023). Behavioral patterns of turbulent kinetic energy budget and quadrant analysis for flows over bedform under the influence of downward seepage. *AIP Advances*, *13*(6), 065331. https://doi.org/10.1063/5.0155757

Beltaos, S. (Ed.) (2008). *River ice breakup*. Water Resources Publications, LLC.

Bennett, K. E., & Prowse, T. D. (2010). Northern Hemisphere geography of ice-covered rivers. *Hydrological Processes*, *24*(2), 235–240. https://doi.org/10.1002/hyp.7561

Blåfield, L., Calle, M., Kasvi, E., & Alho, P. (2024). Modelling seasonal variation of sediment connectivity and its interplay with river forms. *Geomorphology*, *463*, 109346. https://doi.org/10.1016/j.geomorph.2024.109346

Chen, G., Gu, S., Li, B., Zhou, M., & Huai, W. (2018). Physically based coefficient for streamflow estimation in ice-covered channels. *Journal of Hydrology*, *563*, 470–479. https://doi.org/10.1016/j.jhydrol.2018.06.032

Das, V. K., & Debnath, K. (2025). Understanding riverbank erosion through the Lens of Turbulence: A review. *Journal of Hydrology*, *649*, 132484. https://doi.org/10.1016/j.jhydrol.2024.132484

Demers, S., Buffin-Bélanger, T., & Roy, A. G. (2011). Helical cell motions in a small ice-covered meander river reach. *River Research and Applications*, *27*(9), 1118–1125. https://doi.org/10.1002/rra.1451

Demers, S., Buffin-Bélanger, T., & Roy, A. G. (2013). Macroturbulent coherent structures in an ice-covered river flow using a pulse-coherent acoustic Doppler profiler. *Earth Surface Processes and Landforms*, *38*(9), 937–946. https://doi.org/10.1002/esp.3334

De Serio, F., & Mossa, M. (2015). Analysis of mean velocity and turbulence measurements with ADCPs. *Advances in Water Resources*, *81*, 172–185. https://doi.org/10.1016/j.advwatres.2014.11.006

Dey, S. (2014). *Fluvial Hydrodynamics: Hydrodynamic and Sediment Transport Phenomena*. Springer Berlin Heidelberg. https://doi.org/10.1007/978-3-642-19062-9

Ettema, R. (2002). Review of Alluvial-channel Responses to River Ice. *Journal of Cold Regions Engineering*, *16*(4), 191–217. https://doi.org/10.1061/(ASCE)0887-381X(2002)16:4(191)

Ettema, R. (2008). Ice Effects on Sediment Transport in Rivers. In M. H. García (Ed.), *Sedimentation Engineering—Processes; Measurements; Modeling; and Practice*. American Society of Civil Engineers (ASCE).

Ettema, R., & Daly, S. (2004). Sediment Transport Under Ice (Vol. *61*).

Ettema, R., & Kempema, E. W. (2012). River-Ice Effects on Gravel-Bed Channels. In M. Church, P. M. Biron, & A. G. Roy (Eds.), *Gravel-Bed Rivers* (1st ed., pp. 523–540). Wiley. https://doi.org/10.1002/9781119952497.ch37

Finnish Meteorological Institute. (2025). Weather observations [Dataset]. https://en.ilmatieteenlaitos.fi/download-observations

Fukś, M. (2023). Changes in river ice cover in the context of climate change and dam impacts: A review. *Aquatic Sciences*, *85*(4), 113. https://doi.org/10.1007/s00027-023-01011-4

Ghareh Aghaji Zare, S., Moore, S. A., Rennie, C. D., Seidou, O., Ahmari, H., & Malenchak, J. (2016). Estimation of composite hydraulic resistance in ice-covered alluvial streams. *Water Resources Research*, *52*(2), 1306–1327. https://doi.org/10.1002/2015WR018096

Gilcoto, M., Jones, E., & Fariña-Busto, L. (2009). Robust Estimations of Current Velocities with Four-Beam Broadband ADCPs. *Journal of Atmospheric and Oceanic Technology*, *26*(12), 2642–2654. https://doi.org/10.1175/2009JTECHO674.1

Groom, J., & Friedrich, H. (2019). Spatial structure of near-bed flow properties at the grain scale. *Geomorphology*, *327*, 14–27. https://doi.org/10.1016/j.geomorph.2018.10.013

Guo, J., Shan, H., Xu, H., Bai, Y., & Zhang, J. (2017). Exact solution for asymmetric turbulent channel flow with applications in ice-covered rivers. *Journal of Hydraulic Engineering*, *143*(10), 04017041. https://doi.org/10.1061/(ASCE)HY.1943-7900.0001360

Huang, J., Zhang, X., Zhang, Q., Lin, Y., Hao, M., Luo, Y., et al. (2017). Recently amplified arctic warming has contributed to a continual global warming trend. *Nature Climate Change*, *7*(12), 875–879. https://doi.org/10.1038/s41558-017-0009-5

Jafari, R., & Sui, J. (2021). Velocity field and turbulence structure around spur dikes with different angles of orientation under ice covered flow conditions. *Water*, *13*(13), 1844. https://doi.org/10.3390/w13131844

Jamieson, E. C., Post, G., & Rennie, C. D. (2010). Spatial variability of three-dimensional Reynolds stresses in a developing channel bend. *Earth Surface Processes and Landforms*, *35*(9), 1029–1043. https://doi.org/10.1002/esp.1930

Kämäri, M., Alho, P., Colpaert, A., & Lotsari, E. (2017). Spatial variation of river-ice thickness in a meandering river. *Cold Regions Science and Technology*, *137*, 17–29. https://doi.org/10.1016/j.coldregions.2017.01.009

Kasvi, E., Salmela, J., Lotsari, E., Kumpula, T., & Lane, S. N. (2019). Comparison of remote sensing based approaches for mapping bathymetry of shallow, clear water rivers. *Geomorphology*, *333*, 180–197. https://doi.org/10.1016/j.geomorph.2019.02.017

Kasvi, E., Vaaja, M., Kaartinen, H., Kukko, A., Jaakkola, A., Flener, C., et al. (2015). Sub-bend scale flow–sediment interaction of meander bends—A combined approach of field observations, close-range remote sensing and computational modelling. *Geomorphology*, *238*, 119–134. https://doi.org/10.1016/j.geomorph.2015.01.039

Koyuncu, B., & Le, T. B. (2022). On the Impacts of Ice Cover on Flow Profiles in a Bend. *Water Resources Research*, *58*(9), e2021WR031742. https://doi.org/10.1029/2021WR031742

Kumar, P., Deepak, V., & Sharma, A. (2025). Flow dynamics and bed morphology in a narrow channels: A comparative study of experimental and numerical approaches to velocity distribution. *Geomorphology*, *474*, 109645. https://doi.org/10.1016/j.geomorph.2025.109645

Larsen, P. A. (1966). Head losses caused by an ice cover on open channels. *Boston: Boston Society of Civil Engineers*, *56*(NO 1), 45–67. JAN 1969. 23 P, 20 FIG, *4 REF*.

Lentz, S. J., Kirincich, A., & Plueddemann, A. J. (2022). A note on the depth of sidelobe contamination in acoustic Doppler current profiles. *Journal of Atmospheric and Oceanic Technology*, *39*(1), 31–35. https://doi.org/10.1175/JTECH-D-21-0075.1

Lintunen, K. (2025). Near-bed flow turbulence beneath ice cover under varying hydrological conditions: A 9-year field measurement-based analysis from a meander bend - Turbulence values and statistical analyses results [Dataset]. *Zenodo*. https://doi.org/10.5281/zenodo.17984777

Lotsari, E., Dietze, M., Kämäri, M., Alho, P., & Kasvi, E. (2020). Macro-turbulent flow and its impacts on sediment transport potential of a subarctic river during ice-covered and open-channel conditions. *Water*, *12*(7), 1874. https://doi.org/10.3390/w12071874

Lotsari, E., Kasvi, E., Kämäri, M., & Alho, P. (2017). The effects of ice cover on flow characteristics in a subarctic meandering river. *Earth Surface Processes and Landforms*, *42*(8), 1195–1212. https://doi.org/10.1002/esp.4089

Historical Studies, University of Eastern Finland, supported the work financially. Funding was also received from the British Society for Geomorphology (research project title "Defrosting sedimentary systems: the impacts on the evolution and material transport of high-latitude rivers" [registered charity number: 1054260]). Open access publishing facilitated by Turun yliopisto, as part of the Wiley - FinELib agreement.

Lotsari, E., Lintunen, K., Kasvi, E., Alho, P., & Blåfield, L. (2022). The impacts of near-bed flow characteristics on river bed sediment transport under ice-covered conditions in 2016–2021. *Journal of Hydrology*, *615*, 128610. https://doi.org/10.1016/j.jhydrol.2022.128610

Lotsari, E., Tarsa, T., Kämäri, M., Alho, P., & Kasvi, E. (2019). Spatial variation of flow characteristics in a subarctic meandering river in ice-covered and open-channel conditions: A 2D hydrodynamic modelling approach. *Earth Surface Processes and Landforms*, *44*(8), 1509–1529. https://doi.org/10.1002/esp.4589

Lotsari, E., Vaaja, M., Flener, C., Kaartinen, H., Kukko, A., Kasvi, E., et al. (2014). Annual bank and point bar morphodynamics of a meandering river determined by high-accuracy multitemporal laser scanning and flow data. *Water Resources Research*, *50*(7), 5532–5559. https://doi.org/10.1002/2013WR014106

Lotsari, E., Lind, L., & Kämäri, M. (2019). Impacts of hydro-climatically varying years on ice growth and decay in a Subarctic river. *Water*, *11*(10), 2058. https://doi.org/10.3390/w11102058

Mansikkaniemi, H., & Mäki, O.-P. (1990). Paleochannels and recent changes in the Pulmankijoki valley, northern Lapland. *Fennia—International Journal of Geography*, *168*(2), 137–152.

Muste, M., Braileanu, F., & Ettema, R. (2000). Flow and sediment transport measurements in a simulated ice-covered channel. *Water Resources Research*, *36*(9), 2711–2720. https://doi.org/10.1029/2000WR900168

Newton, A. M. W., & Mullan, D. J. (2021). Climate change and Northern Hemisphere lake and river ice phenology from 1931–2005. *The Cryosphere*, *15*(5), 2211–2234. https://doi.org/10.5194/tc-15-2211-2021

Nystrom, E. A., Rehmann, C. R., & Oberg, K. A. (2007). Evaluation of Mean Velocity and Turbulence Measurements with ADCPs. *Journal of Hydraulic Engineering*, *133*(12), 1310–1318. https://doi.org/10.1061/(ASCE)0733-9429(2007)133:12(1310)

Peel, M. C., Finlayson, B. L., & McMahon, T. A. (2007). Updated world map of the Köppen-Geiger climate classification. *Hydrology and Earth System Sciences*, *11*(5), 1633–1644. https://doi.org/10.5194/hess-11-1633-2007

Prowse, T. D. (2001). River-Ice Ecology. I: Hydrologic, Geomorphic, and Water-Quality Aspects. *Journal of Cold Regions Engineering*, *15*(1), 1–16. https://doi.org/10.1061/(ASCE)0887-381X(2001)15:1(1)

Robert, A., & Tran, T. (2012). Mean and turbulent flow fields in a simulated ice-covered channel with a gravel bed: Some laboratory observations. *Earth Surface Processes and Landforms*, *37*(9), 951–956. https://doi.org/10.1002/esp.3211

Salmela, J., Kasvi, E., Vaaja, M. T., Kaartinen, H., Kukko, A., Jaakkola, A., & Alho, P. (2020). Morphological changes and riffle-pool dynamics related to flow in a meandering river channel based on a 5-year monitoring period using close-range remote sensing. *Geomorphology*, *352*, 106982. https://doi.org/10.1016/j.geomorph.2019.106982

Shen, H. T. (2025). River Ice Effects on Sediment Transport and Channel Morphology—Progress and Research Needs. *Glacies*, *2*(1), 2. https://doi.org/10.3390/glacies2010002

Simons, D. B., & Richardson, E. V. (1966). *Resistance to flow in alluvial channels (Report No. 422J; Professional Paper)*. USGS Publications Warehouse. https://doi.org/10.3133/pp422J

Smith, K., Cockburn, J. M. H., & Villard, P. V. (2023). Rivers under Ice: Evaluating simulated morphodynamics through a riffle-pool sequence. *Water*, *15*(8), 1604. https://doi.org/10.3390/w15081604

SonTek. (2013). RiverSurveyor—Discharge, bathymetry and current profiling.

SonTek. (2019). FlowTracker2—User's Manual 1.7.

SonTek. (2022). RiverSurveyor S5/M9—System Manual.

Stacey, M. T., Monismith, S. G., & Burau, J. R. (1999). Measurements of Reynolds stress profiles in unstratified tidal flow. *Journal of Geophysical Research*, *104*(C5), 10933–10949. https://doi.org/10.1029/1998JC900095

Sui, J., Wang, J., He, Y., & Krol, F. (2010). Velocity profiles and incipient motion of frazil particles under ice cover. *International Journal of Sediment Research*, *25*(1), 39–51. https://doi.org/10.1016/S1001-6279(10)60026-1

Sukhodolov, A., Thiele, M., Bungartz, H., & Engelhardt, C. (1999). Turbulence structure in an ice-covered, Sand-bed River. *Water Resources Research*, *35*(3), 889–894. https://doi.org/10.1029/1998WR900081

Sukhodolov, A. N. (2012). Structure of turbulent flow in a meander bend of a lowland river. *Water Resources Research*, *48*(1), 2011WR010765. https://doi.org/10.1029/2011WR010765

Teal, M. J., Ettema, R., & Walker, J. F. (1994). Estimation of mean flow velocity in ice-covered channels. *Journal of Hydraulic Engineering*, *120*(12), 1385–1400. https://doi.org/10.1061/(ASCE)0733-9429(1994)120:12(1385)

Turcotte, B., Morse, B., Bergeron, N. E., & Roy, A. G. (2011). Sediment transport in ice-affected rivers. *Journal of Hydrology*, *409*(1–2), 561–577. https://doi.org/10.1016/j.jhydrol.2011.08.009

Välimäki, J.-M., Lotsari, E., Eltner, A., & Takala, T. (2025). Measuring seasonal bedload transport rates in a sub-arctic river using image processing techniques. https://doi.org/10.5194/egusphere-egu25-18955

Van Rijn, L. C. (1984). Sediment transport, Part III: Bed forms and Alluvial Roughness. *Journal of Hydraulic Engineering*, *110*(12), 1733–1754. https://doi.org/10.1061/(ASCE)0733-9429(1984)110:12(1733)

Vilhonen, E. (2025). Tucaco—Turbulence calculation code (1.0.0) [Computer Software]. *Zenodo*. https://doi.org/10.5281/zenodo.17867164

Wang, F., Huai, W., & Guo, Y. (2021). Analytical model for the suspended sediment concentration in the ice-covered alluvial channels. *Journal of Hydrology*, *597*, 126338. https://doi.org/10.1016/j.jhydrol.2021.126338

Wang, H., Liu, J., Klaar, M., Chen, A., Gudmundsson, L., & Holden, J. (2024). Anthropogenic climate change has influenced global river flow seasonality. *Science*, *383*(6686), 1009–1014. https://doi.org/10.1126/science.adi9501

Wilcox, A. C., & Wohl, E. E. (2006). Flow resistance dynamics in step-pool stream channels: 1. Large woody debris and controls on total resistance. *Water Resources Research*, *42*(5), 2005WR004277. https://doi.org/10.1029/2005WR004277

Yang, X., Pavelsky, T. M., & Allen, G. H. (2020). The past and future of global river ice. *Nature*, *577*(7788), 69–73. https://doi.org/10.1038/s41586-019-1848-1